Production of H_2 by water radiolysis in cement paste under electron irradiation: a joint experimental and theoretical study

Sophie Le Caër[a*], Lucile Dezerald[b,c,d], Khaoula Boukari[e], Maxime Lainé[a], Sébastien Taupin[a,b,c3], Ryan M. Kavanagh[f], Conrad S. N. Johnston[f], Eddy Foy[a], Thibault Charpentier[a], Konrad J. Krakowiak[g,,b], Roland J.-M. Pellenq[b,c,e], Franz J. Ulm[b,c], Gareth A. Tribello[f], Jorge Kohanoff[f], and Andres Saúl[e*]

[a]*NIMBE UMR 3685, CEA, CNRS, Université Paris Saclay, CEA Saclay, F-91191 Gif-sur-Yvette Cedex, France*

[b]*Department of Civil and Environmental Engineering, Massachusetts Institute of Technology, Cambridge, Massachusetts 02139, United States*

[c]*MultiScale Material Science for Energy and Environment, UMI 3466 CNRS-MIT, 77 Massachusetts Avenue, Cambridge, Massachusetts 02139, United States*

[d]*Institut Jean Lamour, Université de Lorraine - CNRS, F-54011 Nancy, France*

[e]*Aix-Marseille University, CINaM-CNRS UMR 7325 Campus de Luminy, 13288 Marseille cedex 9, France*

[f]*Atomistic Simulation Centre, Queen's University Belfast, University Road, Belfast BT9 1NN, UK*

[g]*Department of Civil and Environmental Engineering, Cullen College of Engineering, University of Houston, Houston, Texas 77204-4003, United States*

**Corresponding authors: sophie.le-caer@cea.fr; saul@cinam.univ-mrs.fr*

ABSTRACT

Long-term confinement of nuclear waste is one of the main challenges faced by the nuclear industry. Fission products such as ^{90}Sr and ^{137}Cs, both β^- emitters known to induce serious health hazards, represent the largest fraction of nuclear waste. Cement is a good candidate to store them, provided it can resist the effects of irradiation over time. Here, we have investigated the effects of β^- decay on cement by performing electron irradiation experiments on different samples. We show that H_2 production in cement, the main effect of water radiolysis, depends strongly on composition and relative humidity. First-principles calculations indicate that the water-rich interlayer regions with Ca^{2+} ions act as electron traps that promote the formation of H_2. They also show that holes localize in water-rich regions in low Ca content samples and are then able to participate in H_2 production. This work provides new understanding of radiolysis effects in cements.

Keywords: cement paste; radiolysis; H_2 production; first-principles calculations; reaction mechanisms

1. Introduction

One of the main challenges arising in nuclear waste storage is the design of containers that can ensure a safe confinement of medium-to-long-lived radioelements in geological repositories over thousands of years [1]. These containers will interact with both the radioelements they host and with the environment in which they will be stored. These interactions will alter the physicochemical properties of the materials. These effects need to be evaluated in order to safeguard against future problems that might impact on the confinement of the waste. In the case of closed repositories where humidity is difficult or impossible to monitor, specific damage linked to water interactions such as corrosion [2]; infiltration or leaching can alter the integrity of the confinement. In particular, water-container exchanges are of utmost importance when the host material is porous, which is the case for the cement matrices that are envisioned for the long-term storage of medium-lived fission products such as ^{137}Cs and ^{90}Sr. These two isotopes represent the largest active fraction of civil nuclear waste and are prominent emitters of radiation [3-5]. Hence, it is extremely important to understand what reactions these radioisotopes can induce when they are in contact with cement matrices.

From an industrial point of view, cement-based materials are good candidates to store large quantities of nuclear waste as they are inexpensive, easy to produce and can be tailored to possess a wide range of useful properties. However, assessing the ability of cement to store nuclear waste is a complicated task since it is a material with various possible compositions and a complex nano- and micro- structure [6, 7]. Cement paste is mainly composed of C-S-H (Calcium Silicate Hydrates, the main hydration product of clinker) and portlandite. It also contains residual clinker (that only partially reacted with water during fabrication) such as alite, belite, and ferrite. Cohabitation of these phases results in multiscale porosity and a material made of micrometric sized pores, nanometric gel pores (1-12 nm) and what H. M. Jennings calls “intraglobular pores” (IGPs) [8] that result from the intrinsic disordered layered structure of C-S-H. These IGPs have typical sizes smaller than 1 nm.

The filling of these pores with water depends on the relative humidity (RH) of cement paste [9-11]. The RH value can thus give some insight into the amount of water present in a cement paste sample. At very low RH values, the only water in the cement paste sample is chemically bound water (CBW), i.e. crystallization water and structural water such as –OH groups in the C-S-H interlayer, in IGPs and in other phases such as portlandite [8]. The new water molecules that are introduced upon increasing RH, are referred to as evaporable water (EW) and occupy pores of increasing sizes [8]: for RH values between 11 and 85% water molecules occupy gel pores of sizes up to 12 nm. Meanwhile, when RH exceeds 85%, capillary water molecules (or bulk water) are found in gel pores [8].

In the case of long-term confinement of nuclear waste, the RH value is expected to increase over time in cement containers due to water exchange with the humid host geological media. Furthermore, interaction with ionizing radiation resulting from the radioactive decay of radioelements, will cause radiolysis [12], which leads to H_2 production. It is possible that accumulation of dihydrogen can induce structural damage such as the cracking of the storage medium and that this reaction could be dangerous as H_2 gas could be released in large storage buildings. The ability of cement matrices to store nuclear waste has been widely studied in the past decades from a physical aspect [13]. If the evolution of the mechanical properties and of the structure of the samples were studied after irradiation [14, 15], the reactivity of such systems was hardly investigated [16]. Nevertheless it is of

paramount importance. For instance, ^{90}Sr contamination of cement paste was recently investigated by means of atomic-scale simulations [17]. That study focused on ^{90}Sr and its transmutation into ^{90}Y and ^{90}Zr by β^- decay, and showed that cement paste is a good candidate to store ^{90}Sr and its radioactive daughter nucleus ^{90}Y [17]. The emitted electron will interact with water in the host material which results in a massive variety of chemical reactions. Water radiolysis studies conducted in systems with confined water [18-20] such as clays [21-24] showed that the mechanisms at play can be very different from those observed in bulk water [12]. For this reason, a quantification and understanding of electron-induced H_2 production requires studies in the specific environment.

Here, we investigated the effects of electron irradiation, mimicking β^- emitters, on cement paste by measuring H_2 production under irradiation as a function of relative humidity in several cement paste samples with controlled initial composition. The choice of sample composition aims to give insight into: a) the effect of siliceous (α-quartz) aggregate on the global performance of hydrated oil-well cement systems under electron radiation e.g. for application in deep borehole nuclear waste storage [25, 26], b) to gain qualitative and quantitative insight into radiolysis of low calcium C-S-H, typical of concrete with pozzolanic additives e.g. silica fume [27]. We found that both the relative humidity and the chemical composition of cement paste have a marked influence on H_2 production. Notably, we evidence that H_2 can be produced from the chemically bound water molecules in the C-S-H interlayer pores. This fact was further investigated by means of first principles *ab initio* calculations, which provided insight into the reaction mechanisms for water radiolysis in this confined environment. We studied the effects of adding or removing one electron to C-S-H using two model 11 Å tobermorite structures which are regarded as simple analogues for C-S-H. We show that the excess electron produced by the irradiation-matter interaction has a preference to localize in a region of the tobermorite where structural water is mixed with Ca ions. Hence, the present study helps to understand radiation effects in cements and gives some indications as to what would be the best composition of cement paste for nuclear applications.

2. Materials and Methods

2.1. Experimental setup

Samples preparation To investigate the impact of chemical composition on H_2 production, we prepared three sets of cement paste samples labeled S1, S2, and S3 with controlled compositions.

All samples discussed in this study were prepared from standard American Petroleum Institute Class G cement (Lafarge-Holcim) with typical fineness around 1800 cm^2/g [28]. Quartz (Min-U-Sil 5, d_{50} = 1.5 μm) was added to samples S2 and S3 in the amount of 42% by volume of the blend. This corresponds to the molar ration Ca/Si of the mix equal to 0.83, reflecting the composition of stoichiometric 11Å tobermorite [29]. Cement pastes were synthesized in laboratory conditions at two different water-to-cement ratios (excluding quartz), 0.45 for S1, and 0.54 for S2 and S3 (water-to-binder 0.34). Samples S1 and S2 were hydrated at 25°C under saturated conditions in the lime-saturated water solution for 28 and 84 days, respectively, before being examined. Sample S3 was hydrated at 25°C under saturated conditions for 1 week followed by additional hydrothermal curing at 200°C and 3000 psi (around 21 MPa) for a period of 24h. As a consequence of the different curing procedure, S3 is composed mainly of the low-calcium nano-crystalline C-S-H phase (approximate value of Ca/Si ≈ 0.92 estimated via semi-quantitative XRD) developed in the course of the thermally activated pozzolanic reaction of silica [29, 30]. S1 and S2 contain several phases (hydrated and non-hydrated) and their C-S-H phase is of common stoichiometry 1.7 [29]. In addition to chemical composition, this preparation influences the porosity of the samples: samples S1 and S2 have a multiscale porosity with both gel pores and capillary pores typical of room temperature cured cement paste, while S3, which contains mainly pozzolanic C-S-H, thus does not have capillary pores (see Supporting Information SI 1). Furthermore, the use of a larger water to cement ratio to prepare S2 combined with the absence of high temperature curing leads to larger fraction of capillary pores in cement matrix of S2 than for S1 [29, 31].

As silica-enriched cements such as S2 are envisioned for nuclear waste storage [32], comparing S1 with S2 will provide an insight into the effect of silica aggregate on the performance of Portland cement-based matrices under long-term exposure to electron radiation. S3 will shed light on H_2

production by C-S-H mainly and will provide a good representation of how cement containers will behave over long periods of time. This point is especially relevant in the context of nuclear waste storage, since cement paste continuously cures until stabilization of a single C-S-H phase whose properties are close to torbermorite with Ca/Si = 0.86 [33].

The three cement pastes were first ground into powder. For each set, several samples with different relative humidity (RH = 0%, 11%, 43%, 74% and 97%) were prepared to evaluate the influence of the relative humidity on H_2 production. All samples were placed in an air-tight chamber with an environment of a known relative humidity created by a saturated salt solution until equilibrium is reached: 0% (dried at 110°C for two days and then placed in the desiccator containing silica gel [34]), 11% (LiCl saturated solution), 43% (K_2CO_3 saturated solution), 74% ($NaNO_3$ saturated solution) and 97% (K_2SO_4 saturated solution). Sample weight stability over at least one week attested that the equilibrium state was reached in the chamber.

Samples characterization. All samples were characterized before and after irradiation, for each investigated RH. The macroscopic crystalline phases contained in each sample were determined by X-ray Diffraction (XRD) performed with a rotating anode X-ray generator. The beam was delivered by a Molybdenum anode ($\lambda K_{\alpha 1}$ = 0.70932 Å). XRD patterns were collected by a 2D image plate detector. Classical I = f(2θ) powder XRD patterns were obtained after circular integration of the diffracted image using the FIT2D program. The data is shown in Supporting Information SI 2. They were confirmed by infrared spectroscopy presented in Supporting Information SI 3.

Quantitative analysis of the samples composition was performed using Thermogravimetric Analysis – Differential ThermoGravimetry (TGA-DTG) measurements with a Mettler-Toledo TGA/DSC 1 analyzer. The samples (approximately 20 mg) were placed in an alumina crucible of 70 µL and heated from 25 to 1000 °C at a ramp rate of 10 °C min^{-1} under a dinitrogen flux of 50 mL min^{-1} and then cooled down to room temperature. Data was analyzed using the STAR^e software. This method allows the quantity of water in each sample, and whether the water is evaporable (weight loss between ambient temperature and 105˚C [35]) or chemically bound water, to be evaluated. It also detects the

presence of the following hydrated phases: portlandite, ettringite, tricalcium monosulpho-aluminate (hereafter called AFm) and C-S-H (see Table 1 for the chemical formulas of the species). The exact amount of portlandite was measured since it is known to produce a peak between 410 and 500˚C [30]. An approximate value for the quantity of ettringite was obtained from TGA by considering that the loss around 110˚C corresponds to the release of 27 water molecules [36]. The exact quantity of C-S-H and AFm could not be determined, however, as the determination of the percentage of the former with TGA with a correct uncertainty can be challenging and the quantity of the latter is known to be very low in the samples [37]. In addition to measuring the presence of the hydrated phases, TGA also measures the quantity of calcite when the samples were carbonated. In that case, decarbonation of the samples produces a DTG peak between 550 and 800˚C that enabled us to evaluate the quantity of calcite in the samples [38]. Details of the TGA-DTA results and analysis are given in Supporting Information SI 4.

H_2 production measurement In order to prepare the samples for irradiation, approximately 300 mg were placed in a Pyrex glass ampoule (about 10 mL) that was outgassed with a primary pump and then subsequently filled with 1.55 bar of Argon 6.0 (99.9999%). This operation was repeated three times before the first irradiation step and then once between each irradiation step. The same outgassing procedure was performed on a non-irradiated sample to be used as a reference. Irradiation was performed using 10 MeV electron pulses of a Titan Beta, Inc. linear accelerator (LINAC) [39]. The duration of the pulse is 10 ns and the repetition rate was set to 2 Hz in order to avoid any macroscopic heating of the sample during irradiation. The dose per pulse (30 ± 2 $Gy.pulse^{-1}$) was determined by Fricke dosimetry [40]. The dose determined this way is considered to be the same as the dose received by the cement paste samples. The H_2 produced under irradiation was measured by gas chromatography (μGC-R3000 SRA Instrument) using ultra-high purity argon as a carrier gas. Prior to the analysis, the gas contained in the ampoule was diluted in Argon 6.0 at a total pressure of 1.5 bar for five minutes to ensure a homogeneous mixing between gases.

2.2. Computational details

First principles electronic structure calculations were carried out to investigate the effects of adding or removing one electron to C-S-H using two 11 Å tobermorite (TBB-11) structures [41]. This atomic-scale model was chosen because TBB-11 is known to be a good model for C-S-H with a low Ca/Si ratio [41] as it is the case here for sample S3. The calculations were performed using the CP2K package [42] that implements the Gaussian and Plane Wave (GPW) [43] Density Functional Theory (DFT) approach in a module known as Quickstep [44]. Molecularly optimized atom-centered Gaussian basis sets [45] were used with a plane wave cutoff of 500 Ry. Two types of calculations were performed: static DFT and DFT Molecular Dynamics (DFTMD) calculations. For both calculations, we used the Minnesota hybrid (M06-2X) [46] functional that enables the excess electron (as well as the electron-hole) to localize in the cell, which does not occur with standard functionals such as the Perdew-Burke-Ernzerhof (PBE) generalized-gradient approximation (GGA) functional [47]. Norm-conserving, separable, dual-space Goedecker-Teter-Hutter pseudopotentials [48, 49] re-optimized for the PBE exchange-correlation functional [47] were employed. Dispersion effects were included using the empirical DFT-D3 pair potential [50, 51]. For spin polarized calculations, the Unrestricted Kohn-Sham (UKS) [52] formalism was used for both functionals. Periodic boundary conditions were used for all calculations. For the Hartree-Fock exchange calculation needed for the hybrid functional, a truncated Coulomb operator was used [53, 54], in conjunction with the efficient Auxiliary Density Matrix Method [55].

The initial (neutral) TBB-11Å cells were first relaxed with PBE-GGA functional using the Quantum ESPRESSO package [56] which implements DFT by using a plane wave basis and pseudopotentials. The simulation was then continued using the same code by performing DFTMD calculations in the NVE ensemble for about 200 fs with a time step of 1 fs. The final structure was further relaxed using the PBE-GGA functional. These calculations were terminated once the forces on the atoms were smaller than 10^{-3} Ry/a_0. Then, starting from this new geometry, the system was relaxed with an excess electron using the M06-2X functional with the CP2K code using a m-TZV2P basis (with the exception of calcium, which had a m-DZVP basis throughout) and the PBE functional. In order to check the

stability of the excess electron at finite temperatures, DFTMD calculations were carried out using CP2K with the presence of an excess electron, and in a separate calculation, an additional hole. The system was simulated using the NVT ensemble and thermostated at 300 K using the canonical sampling through velocity rescaling algorithm [57]. The equations of motion were integrated using the standard velocity Verlet algorithm with a time step of 0.5 fs, and the wavefunction was extrapolated between steps using the time reversible Always Stable Predictor-Corrector algorithm [58]. This entire procedure was repeated separately with an electron and a hole.

3. Results and discussion

3.1. Samples composition

The different phases present in samples S1-3 before and after irradiation were determined by XRD. The main phases found are presented in Table 1, and the detailed XRD analysis is given in Supporting Information SI 2. The Si-containing phases were investigated thanks to ^{29}Si NMR and the corresponding results are given in Supporting Information SI 5. We found C-S-H in all samples, which is to be expected as it is the main hydration product of clinker. Sample S3 is mainly composed of C-S-H (see Supporting Information SI 5). Samples S1 and S2 contain ettringite (except at the lowest RH), AFm, and portlandite. None of these phases were found in S3, i.e., the only hydrated phase in S3 is C-S-H as expected from the sample preparation. Since clinker never entirely reacts with water, we also found non-hydrated phases such as ferrite and alite in all samples; as well as belite in S1 and S2. The amount of anhydrous phases is low in S2 and S3 as compared to S1 (Supporting Information SI 1). Quartz was also found in S2 and S3, as expected. However, quartz is present in very low amount in S3 as compared to S2 (see Supporting Information SI 5). XRD showed that all the samples also contain calcite, which is unexpected since the preparation of the samples was designed to avoid carbonated phases. Calcite is commonly found in cement paste since it strongly absorbs CO_2 from the atmosphere. In our case, carbonation of the samples most likely occurred in the desiccators.

	S1	S2	S3
Hydrated Phases			
Calcium Silicate Hydrates (C-S-H, $CaO\text{-}SiO_2\text{-}H_2O$)	X	X	X
Ettringite ($3CaO{\bullet}Al_2O_3{\bullet}3CaSO_4{\bullet}32H_2O$)	X	X	
Tricalcium monosulpho-aluminate (AFm, $3CaO{\bullet}Al_2O_3{\bullet}CaSO_4{\bullet}12H_2O$)	X	X	
Portlandite ($Ca(OH)_2$)	X	X	
Non-hydrated Phases			
Alite ($3CaO{\bullet}SiO_2$)	X	X	X
Ferrite ($4CaO{\bullet}Al_2O_3{\bullet}Fe_2O_3$)	X	X	X
Belite ($2CaO{\bullet}SiO_2$)	X	X	
Quartz (SiO_2)		X	X
Calcite ($CaCO_3$)	X	X	X

Table 1. *Samples composition as detected with XRD. The samples composition given here was confirmed using FT-IR (a similar table is given in Supporting Information SI 2).*

Since the present work focusses on H_2 production, we evaluated, when possible, the quantity of the hydrated phases as well as the quantity of chemically bound water (CBW, i.e. crystallization water and structural water) and evaporable water (EW) for each sample and RH. The quantity of the phases determined by TGA is presented in Fig. 1a. It shows that the calcite content is generally low (below 5%) for all samples with the exception of S1 at 74% RH and S2 at 74 and 97% RH where it is larger than 10%. The largest mass percentages for calcite (above 20%) are found at 74% RH, a level of RH known to favor cement paste carbonation [59]. The only sample for which the calcite content remains at low levels when the RH is 74% is S3, which contains no ettringite or portlandite, in good agreement with the XRD results from Tab. 1. For all samples, we found no ettringite at 0% RH, when AFm is detected [60]. This is expected since fewer water molecules are needed to form AFm than ettringite (see chemical formulae from Tab. 1). A constant amount of ettringite was measured for RHs larger than 11% in S1 and S2. The quantity of ettringite is the largest in S1, and the lowest in S2, as expected due to the incorporation of quartz in S2 and hence, dilution. For a given sample (S1 or S2), the quantity of portlandite varies little with RH as well. The exceptions are S1 at 74% RH where the portlandite content is 40% smaller than for other RHs and S2 where no portlandite is detected at 74% RH and its content at 97% is half the content found for RHs below 43%. In general, portlandite is known to react with CO_2 to form calcite [38], which can explain why no portlandite is detected in S2

at 74% where the calcite amount is the largest (see Fig. 1a). Calcite can also be formed from C-S-H [61] as evidenced in the case of S3. Similarly to ettringite, and for the same reasons, the mass percentage of portlandite is, on average, larger in S1, and lower in S2. Fig. 1b shows the mass percentage of water under its two forms, CBW and EW, as detected with TGA. For all samples, considering the error bars, the CBW content can be considered as being constant with RH. At 0% RH, there is almost no EW (less than 0.7%), which is coherent with the fact that the samples are dried. In all samples, the amount of EW globally increases with increasing RH.

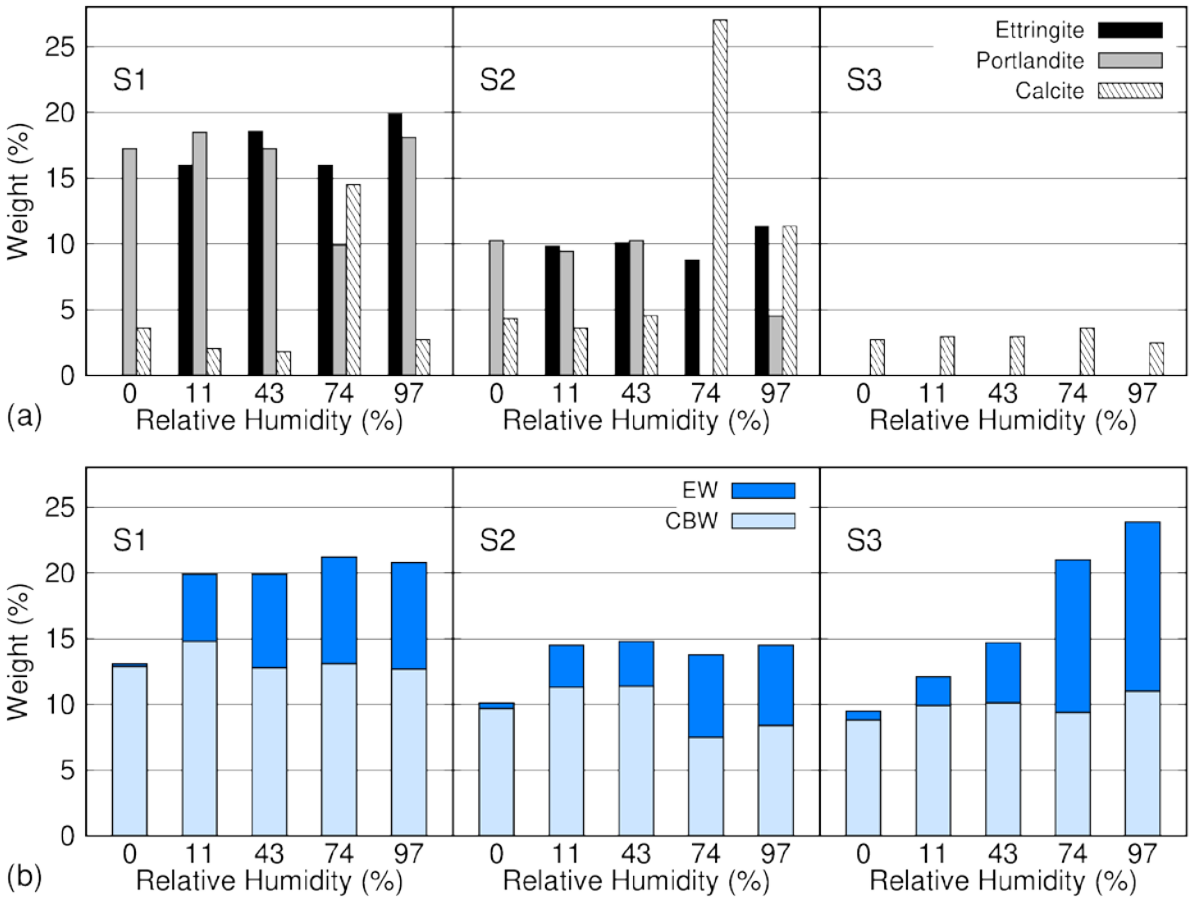

Fig. 1. *Mass percentage (a) of the main phases (ettringite, portlandite and calcite) and (b) of water (evaporable water, EW; and chemically bound water, CBW) as determined from TGA measurements in samples SI 4 as a function of relative humidity. The mass percentage of ettringite has been approximately evaluated (see Supporting Information SI 4). The error bars are estimated to be 15% in all cases except ettringite for which the error bar is even larger. The amount of ettringite is difficult to*

determine and is overestimated due to the presence of other phases as AFm, C-S-H… that lose also weight in this temperature range.

3.2. Radiation-induced H_2 production

All samples were irradiated with four doses at all relative humidity levels examined. When exposed to ionizing radiation, all samples produced H_2. We found no H_2 in non-irradiated samples, so the measurement of H_2 is considered to be a good reference for evaluating the extent to which reactions were induced by irradiation. For all samples, no significant difference in composition before and after irradiation could be evidenced by any of the experimental methods used here (see Supporting Information SI 6) concerning both the quantity of phases and the amount of CBW and EW. This means, in particular, that the global amount of water is not affected by our experimental conditions and that only a small amount of water is affected by the ionizing radiation. This means also that the compositions detailed in Fig. 1 remain the same after irradiation and, as such, we will use this composition in the following when discussing the H_2 production results.

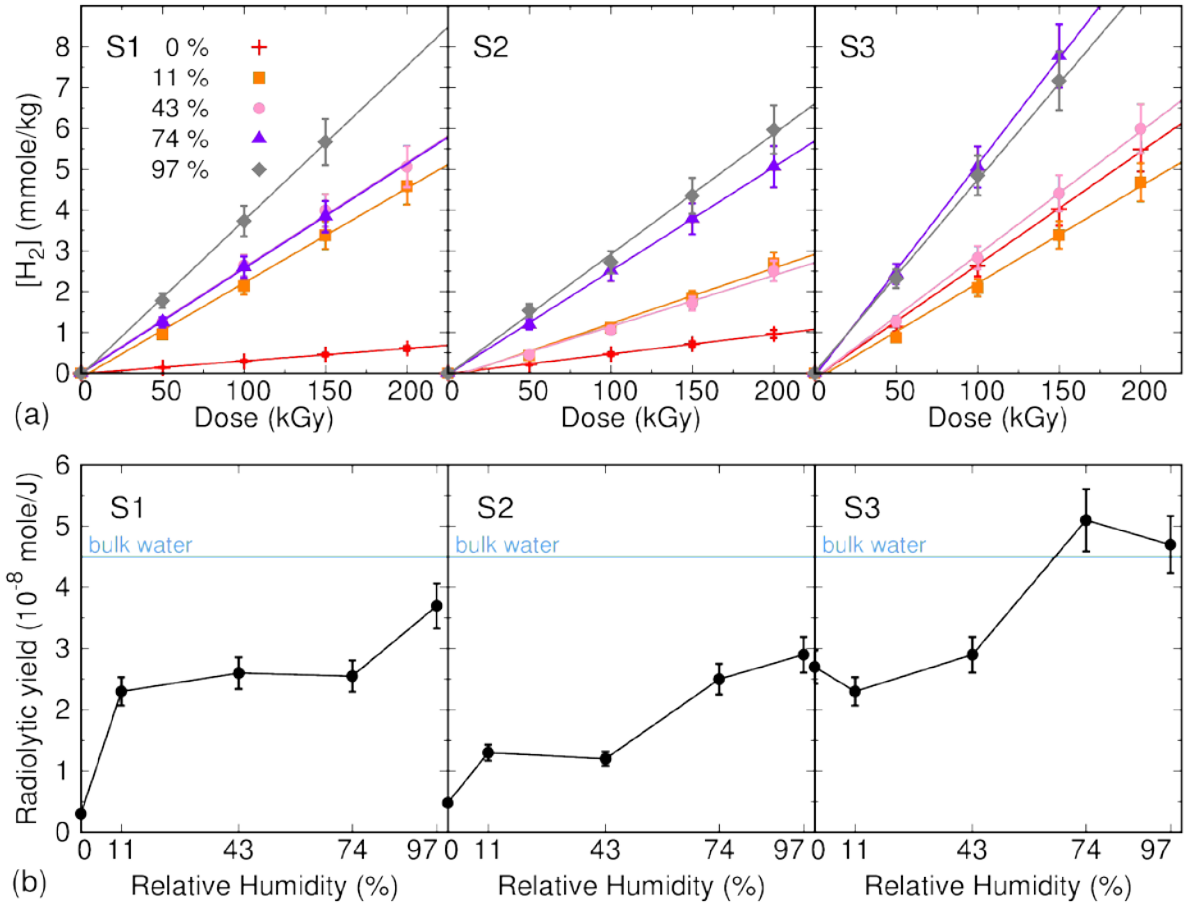

Fig. 2. *(a) Cumulated H_2 production (points) as a function of the cumulated dose and RH for the three samples. The lines correspond to linear fits used to evaluate the radiolytic yields. (b) H_2 radiolytic yield variations with RH for all samples. The full horizontal line corresponds to the H_2 yield measured in bulk water (4.5 10^{-8} mol J^{-1}) at pH 13 [12]. The yields are calculated with respect to the energy deposited in the whole cement paste-water system. The error bars are estimated to be 10%. The radiolytic yields in molecule per 100 eV can be obtained by dividing the value in µmol J^{-1} by 0.10364.*

The evolution of H_2 as a function of dose is given in Fig. 2a. The quantity of H_2 produced increases linearly with the dose. The amount of H_2 produced also increases with increasing RH. To further analyze this data, we report the radiolytic yields for each sample, at each RH, from the slopes of the lines. The yields were calculated with respect to the total mass of cement paste and water, which corresponds to the fact that energy is deposited in the whole system. The radiolytic yields obtained are presented in Fig. 2b. This figure shows that H_2 yields increase as a function of RH, except for those

from samples S1 and S2 for which plateaus are observed between 11 and 74% RH and between 11 and 43% RH, respectively. The H_2 yields are the highest in the case of sample S3, for values of 74 and 97% RH. These yields are similar to those of H_2 in bulk water, implying that efficient H_2 production mechanisms take place in this sample. Confinement effects at the nanometer scale in sample S3 are likely responsible for the yields at 74 and 97% RH being higher than the one in bulk water as recently reported in the case of swelling clays for which the thickness of the interlayer space (a few Å) enables efficient recombination reactions between species [24]. Finally, the H_2 yields are the smallest in sample S2 as the largest measured H_2 yield (at 97% RH) is close to the H_2 yield of sample S1 at 74% RH or even S3 at 0% RH. These results show that silica-enriched cement paste (S2) is more resistant to H_2 production than S1, which is due to the fact that it contain less water molecules (Fig. 1 and Supporting Information SI 7). However, over time, H_2 production is expected to increase drastically since silica-rich cement pastes end up with a composition close to S3 where a higher H_2 production yield is measured.

A more detailed analysis of Fig. 2b along with Fig. 1 provides further insights into the role played by the phases in H_2 production. In sample S2 for example, the plateau between 11 and 43% RH in Fig. 2 is consistent with the fact that the EW content, i.e., the amount of water that is most likely to produce H_2 as compared to CBW [19, 20], is also constant between 11 and 43% RH (Fig. 1b). However, this explanation alone is flawed as, for that same sample, Fig. 1b shows that the quantity of EW is also constant between 74 and 97% while the radiolytic yields from Fig. 2b increase slightly between 74 and 97% RH. This means that an additional mechanism influences radiolytic yield variations in S2. When looking at composition of sample S2 in Fig. 1a, one can see that it changes drastically between 74 and 97% RH, the main difference being the larger quantity of calcite found at 74% RH compared to 97% RH. From these observations, it seems plausible that calcite inhibits H_2 production since, for a constant amount of EW, more H_2 is produced when the calcite amount is smaller (at 97% RH). This result is in good agreement with Ref. [62] which showed that electrons and holes are trapped by calcite using electron paramagnetic resonance experiments performed at 77K after X-irradiation of calcite samples. Moreover, the presence of calcite will also lead to the presence of carbonate anions in the

liquid phase and these anions are known to trap electrons. Considering sample S1, one can draw similar conclusions regarding the role of calcite. For this sample, the radiolytic yield in Fig. 2b increases between 74 and 97% RH although the EW amount is constant. The main difference arises again from the calcite content that is 6 times larger at 74% RH than at 97% RH. Furthermore, the radiolytic yield plateau between 11 and 74% in Fig. 2b coincides with an increasing quantity of EW (Fig. 1b). By comparing the compositions of sample S1 between 11 and 74% RHs (for which the EW content difference is large), one can see that the largest variations in composition corresponds to calcite content again (Fig. 1a). Note that the variations in ettringite and portlandite content between 11 and 43% RH (for which the calcite content is similar and low and the EW content increases) suggest that one or both of these two phases play a role in H_2 production. To discriminate between the role of ettringite and portlandite, it is interesting to compare the H_2 radiolytic yields of samples S1, S2 and S3 at 0% RH, when no ettringite is detected and the amount of EW is lower than 0.7% (Fig. 1). In sample S3, where there is no portlandite, the radiolytic yield at 0% RH is as high as half the radiolytic yield of water whereas in samples S1 and S2 that contain portlandite, the radiolytic yield is close to zero [63]. This suggests that portlandite, similarly to calcite, inhibits H_2 production. This behavior of portlandite under electron irradiation is consistent with former measurements performed under γ irradiation, where it was shown that H_2 production in portlandite is 2.25 times lower than in bulk water [64]. Lastly, the comparison of the H_2 yields at 0, 11 and 43% RH (for which the calcite amounts in S1 and S2 are similar) obtained in S1 and S2 demonstrates the inhibitor role played by quartz, as even if ettringite and portlandite are present in smaller amounts in S2 than in S1, the H_2 yields measured are smaller in S2 than in S1 (Fig. 2b). To take into account the differences in water amount between the different samples at the different relative humidities, the evolution of the H_2 radiolytic yield is given in Supporting Information SI 7 as a function of the EW content. This representation illustrates the discussion above with the influence of the different phases. This is not surprising, as quartz does not possess any hydrogen atoms. It is known, however, that quartz produces defects under irradiation [65]. The same behavior can be expected from the other non-hydrated phases present in the samples.

It is worth noting that in irradiated zeolites [66] the H_2 radiolytic yield is lower than 10^{-8} mol J^{-1} at the lowest water content whereas here, the yield we determine in dry S3 is significantly higher than this value. At this low water content, water is immobilized in the cages of zeolites while it is confined, but mobile in the 2D interlayer space of cement paste. We can therefore assume that the strong interaction of water with the zeolite cages is responsible for the smaller H_2 radiolytic yield value in this system compared to S3. It is also important to point out that, in synthetic clay minerals, the H_2 radiolytic yields can be increased by a factor of 2-3 under high dose rate electron irradiation as compared to the one measured in water, due to very efficient recombination processes taking place in the highly confined interlayer space [24]. Here we do not measure such high H_2 yields, even in S3, which can be partly attributed to the presence of quartz and of anhydrous phases (see Supporting Information SI 5).

The fact that the radiolytic yield is large in S3 at 0% RH, i.e. when the major source of water in the sample is CBW from C-S-H, indicates that the water and –OH groups responsible for the cohesion of the C-S-H phase undergo radiolysis.

The electron-hole pair produced this way deposits energy in the material. Some of this energy can be transferred to water and –OH groups, leading to the breaking of O–H bonds which is the first step of H_2 production by water radiolysis [20]. C-S-H has a layered atomic structure, where the water and –OH groups are confined between silicate chains. At this scale, the nanostructure of C-S-H is very similar to the nanostructure of clays where it has been shown that the thickness of the sheets (less than 1 nm) prevents the formation of an exciton from the electron and hole produced by ionizing radiation [21, 22]. Specific electron and hole interactions with water and –OH groups can thus be expected in C-S-H as well, leading to H_2 production in sample S3 in the absence of EW. Note that the pH of water in paste is around 13, meaning that hydroxide ions are present. Nevertheless, the radiolytic H_2 yield is similar at pH 7 or 13 [12, 16].

3.3. H_2 production mechanism in C-S-H.

The first reaction steps in H_2 production in C-S-H were investigated by means of first principles calculations based on Density Functional Theory (DFT). For this study, C-S-H was modelled as 11 Å

tobermorite (TBB-11, see Fig. 3) as proposed by Merlino et al. [41], which has been shown to be a good model for C-S-H with a low Ca/Si ratio. We have chosen two models that are a good match for sample S3, for which we have experimentally observed efficient H_2 production. These models were chosen as tobermorite has been shown to possess a wide range of chemical compositions based on charge balance, as suggested by Biagioni et al. [67] The general formula of tobermorite without aluminum can be written as:

$$Ca_{4+x}Si_6O_{15+2x}(OH)_{2-2x} \cdot 5H_2O$$

where $0 \leq x \leq 1$, such that x represents the amount of additional calcium incorporated in the tobermorite structural cavities. The high calcium content model presented in this work contains the maximum amount of structural calcium (x = 1), has a chemical constitution of $Ca_{10}Si_{12}O_{34}\cdot 10H_2O$ and a Ca/Si ratio of 0.83, similar to sample S3. We call this model CS-083, and its structure is shown in Fig. 3a. The second model, that represents tobermorite found in the Urals, Russia, corresponds to the x = 0.5 case, such that the chemical formula is $Ca_9Si_{12}O_{32}(OH)_2\cdot 10H_2O$ with a Ca/Si ratio of 0.75. We name this model CS-075, and its structure is shown in Fig. 3b. These models contain 86 and 87 atoms, respectively, and possess Ca/Si ratios that are within the range of experimental values for 11 Å tobermorite (0.67–0.83) [41, 67]. The cells contain silicon atoms in two distinct tetrahedral environments that form silicate chains SiO_4^{4-}. These can be denoted as pairing and bridging tetrahedra where pairing tetrahedra are bound to two other silicate species in the chain, while the bridging groups are linked to three other silicates and form links between chains (Fig. 3a). Calcium is also present in two distinct environments; the intralayer region between two silicate chains, and the interlayer region in which the Calcium is mixed with water and –OH groups (Fig. 3a and 3b). The tobermorite structures chosen contain two interlayer spaces, or pores, and the calcium content of the pores is where the two models differ. The CS-083 model contains one calcium in each interlayer pore, whereas the CS-075 model contains one calcium in one pore only. The location of this calcium was determined by optimizing the geometry via Quantum ESPRESSO calculations. Interestingly, in the CS-083 model, one of the original water molecules in the structure dissociates during the DFTMD equilibration, transferring a proton to one of the SiO_4 tetrahedra and remaining as an OH^- ion.

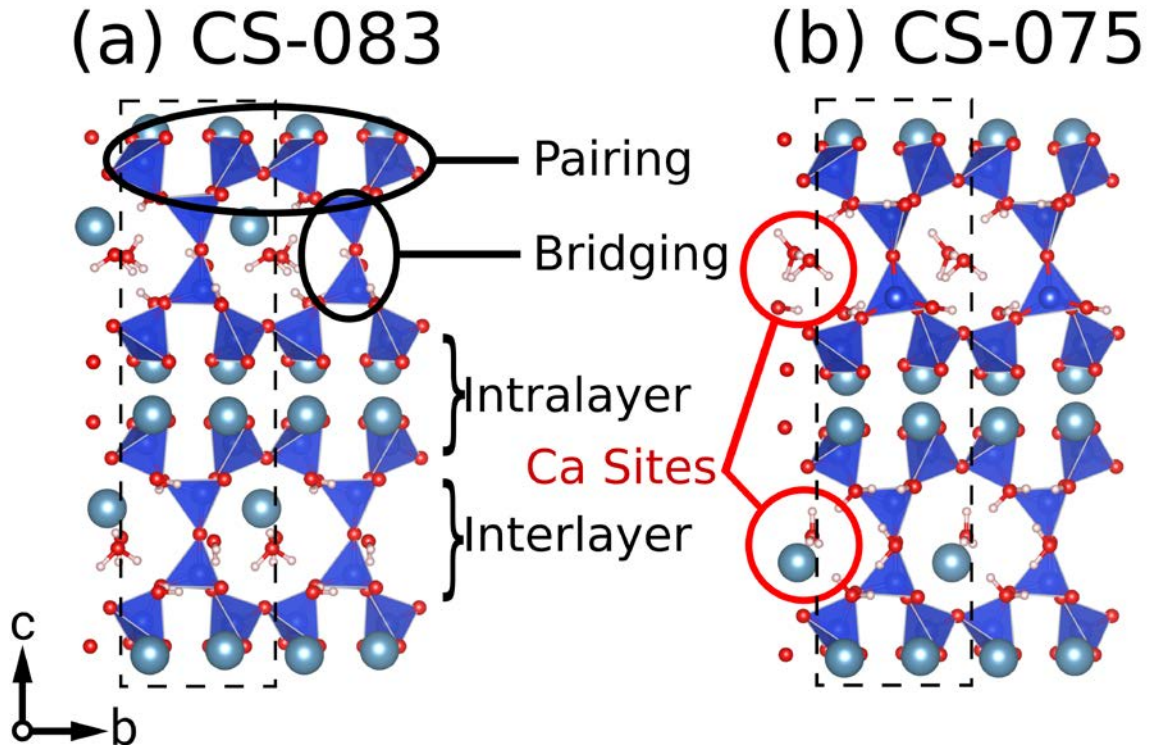

Fig. 3. *a) Atomic structure of CS-083 Model TBB-11Å,(b) Atomic structure of the CS-075 model. Note that only alternating Ca sites are filled due to a partial occupancy of 50%. In both models, calcium, oxygen, hydrogen atoms and silicate chains are represented in grey, red, white and dark blue tetrahedral respectively. The unit cell was doubled in the b direction for clarity. The unit cell for calculations is represented by a dashed line. Both models have been optimized at the M06-2X level. The height of the structures represented is 2.2 nm.*

The excess electron and hole produced by irradiation were modeled by addition or removal of an electron in the simulation cells, respectively. The CS-083 model corresponds roughly to sample S3 at 0% RH after electron irradiation, where water is mainly CBW in the C-S-H interlayer and with almost no EW (Fig. 3a). The CS-075 model also contains only CBW. The addition or removal of an elementary charge from the simulation cell, which is otherwise neutral, leads to a non-zero spin density. This is the case because the neutral system has an even number of electrons and an energy gap, and the additional electron occupies the LUMO in one of the spin projections. The spin density thus corresponds to the electronic density of the excess electron. A similar argument can be applied to the hole. The spin densities obtained for the CS-083 model are plotted along with the simulation cells

in Fig. 4a for the excess electron and in Fig. 5a for the hole, while those for CS-075 tobermorite are shown in Fig. 4b and 5b, respectively.

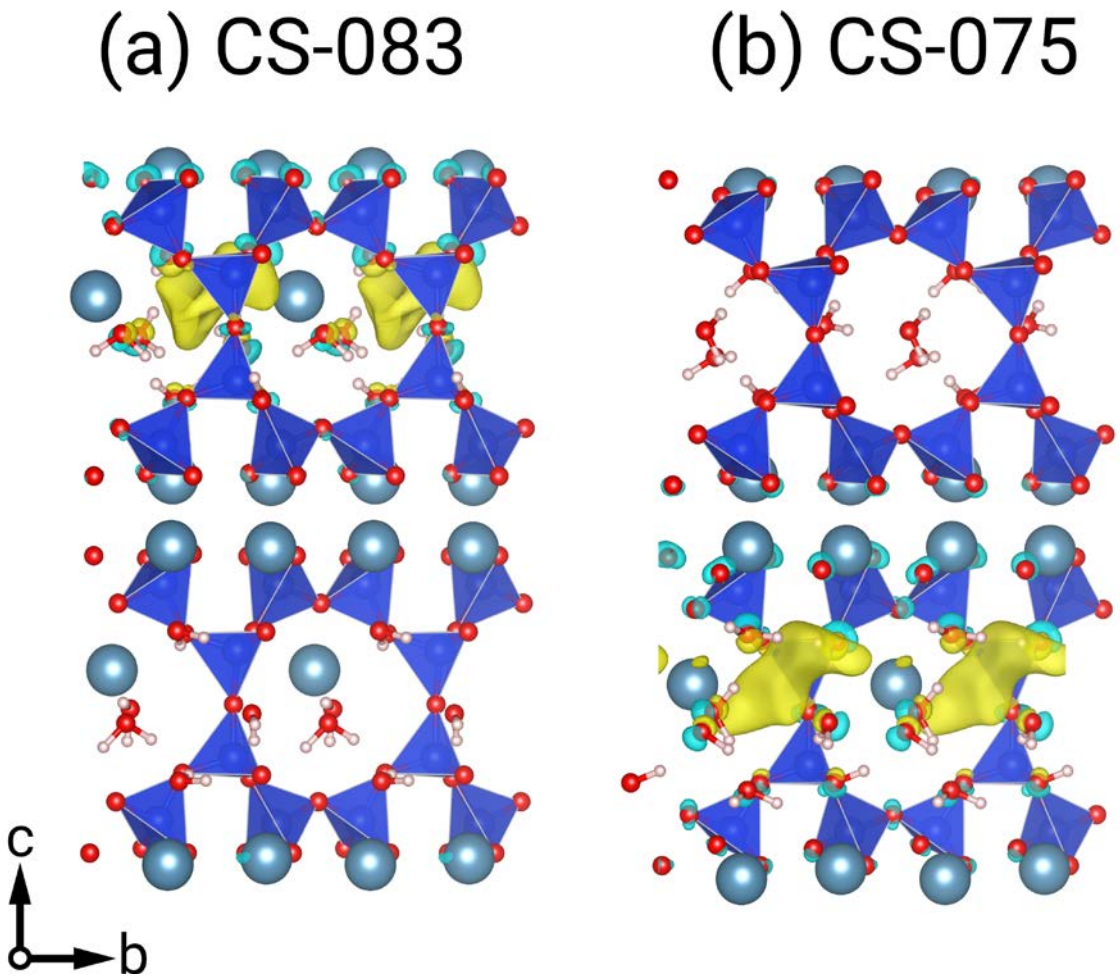

Fig. 4. *Details of: (a) The spin density for the CS-083 model with an excess electron. (b) The spin density for the CS-075 model with an excess electron. Isosurfaces of positive and negative spin densities (± 0.002 e.A^{-3}) are represented in yellow and blue, respectively. In both cases the structures have been optimized at the M06-2X level.*

Fig. 4a shows that the electron localizes in the interlayer region of CS-083 TBB-11 Å, i.e., the region where structural water and OH groups coexists with Ca ions. The additional electron is thus correctly located to subsequently interact with water. The excess electron simulations for the CS-075 model (Fig. 4b) largely agree with the CS-083 model in that the charge can be found in the interlayer space that contains calcium. The electron can mainly be found on the interlayer calcium and a nearby

hydroxyl species which forms part of a Si-OH group in a bridging tetrahedron. The proximity of the water molecules to the Ca ions in the interlayer regions where the electron localizes implies that the electron prefers to be solvated in the interlayer environment containing Ca. Electrons, although they are a strongly reducing species, do not reduce Ca ions, as already pointed out in the case of clay minerals, but prefer to be solvated instead [22]. This is particularly evident in the CS-075 model, where the excess electron localizes in the Ca-rich interlayer spacing. The solvated electron is then a well-known precursor of H_2, as in the case of the reaction of two solvated electrons with each other.

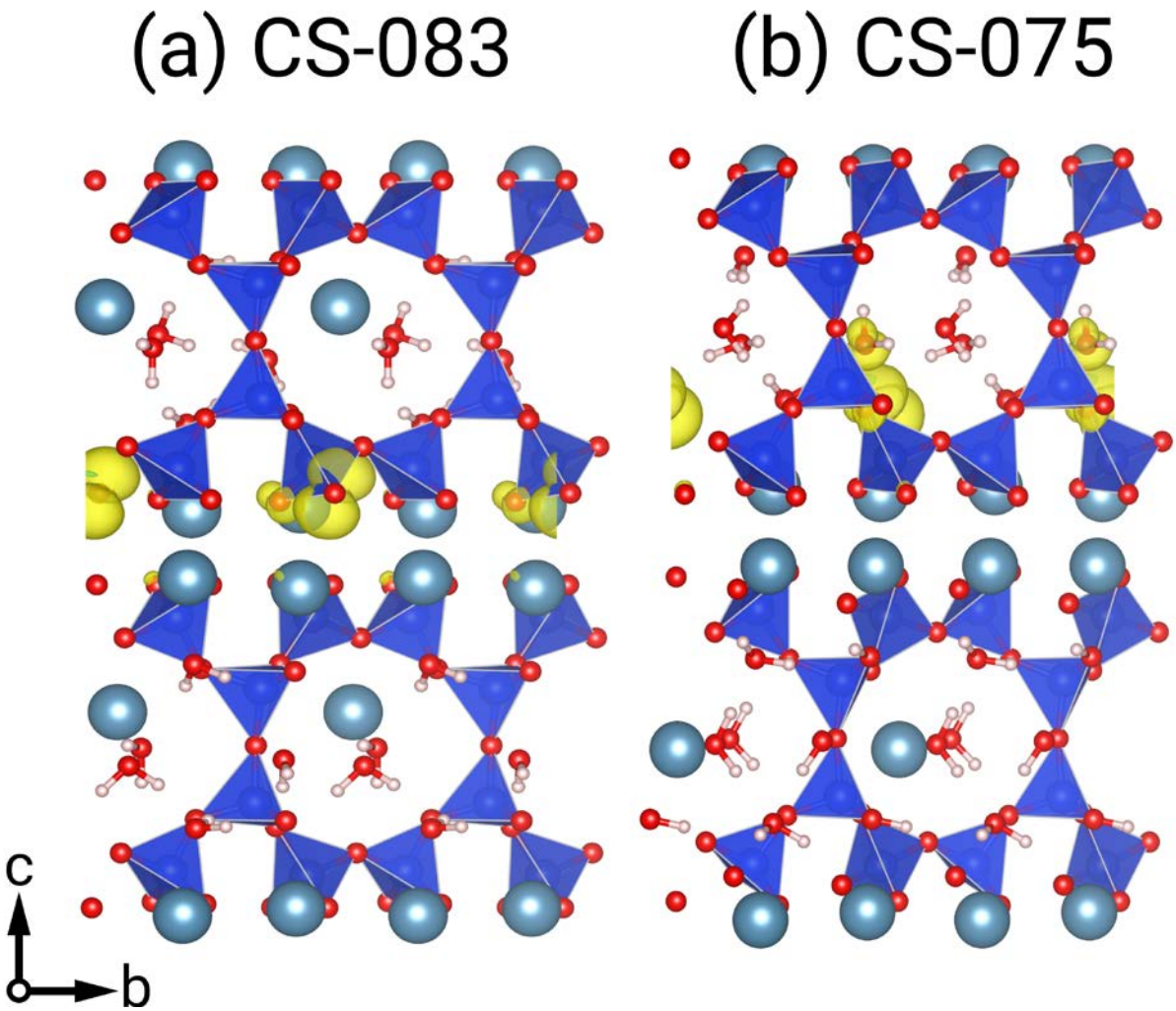

Fig. 5. *Details of: (a) The spin density for the CS-083 model with a hole. (b) The spin density for the CS-075 model with a hole. Isosurfaces of positive and negative spin densities (± 0.002 e.A^{-3}) are represented in yellow and blue, respectively. In both cases the structures have been optimized at the M06-2X level.*

The spin density of CS-083 TBB-11 Å with an additional hole (or removal of an electron) is presented in Fig. 5a. This figure shows that the spin density is mainly localized on the SiO_4 tetrahedral oxygen atoms in the intralayer space. In this case, only 2 oxygen atoms have non-negligible spin moments of 84% and 6% of the total density respectively. The intralayer region does not contain water molecules. We suggest then, that, in the Ca-rich case, the production of H_2 is mostly due to the additional electron, which is localized in the interlayer space and surrounded by water. The hole calculation for the CS-075 model (Fig. 5b), provides slightly different results. The hole appears to localize mainly on a single oxygen which forms part of a SiO_4 tetrahedron in the interlayer spacing. A significant localization of spin can be observed, as 86% of the magnetic moment is associated to this single oxygen. A small fraction, of around 6%, is also found on the nearest water molecule. After reaction with a water molecule, this hole will likely lead to the formation of H^+, and then to hydrogen atom (precursor of H_2) after reduction by an electron. The hole likely localizes in this space due to the "available" electron lone pairs found on the oxygen in question, as it possesses only a single Si-O bond.

The results suggest that the electrons are preferentially localized in the interlayer region with Ca ions and filled with water, while the electron holes are predominantly caught by electron rich oxygen species that make up the tobermorite crystal structure. In either case, these electronic defects provide a means to produce charged species and radicals. In the models tested, the absence or presence of interlayer calcium not only affects the geometry, but the behavior that results from the addition or removal of electrons. We argue that the chemically bound water surrounding the interlayer Ca is susceptible to give rise to H_2 gas as a result of irradiation. This would explain why H_2 production mechanisms can be observed in C-S-H, even when the samples are dried to 0% RH as we observed experimentally.

4. Conclusion

A joint experimental and theoretical study was performed to determine the reaction mechanisms that take place when cement paste is bombarded by ionizing radiation. A systematic evaluation of H_2

production under electron irradiation was performed as a function of the relative humidity and composition of cement pastes. . C-S-H, the main hydration product of clinker that is responsible for paste cohesion and strength, was shown to possess highly efficient H_2 production mechanisms leading to radiolytic yields half as large as the radiolytic yield of bulk water at the lowest RH. Using DFT calculations, we have demonstrated that these mechanisms are likely to be connected to the presence of calcium in the interlayer space of C-S-H, which attracts and traps the electron in an environment filled with water. The electron can then solvate, which can be thought of as the first step towards H_2 production. Its oxidative counterpart, the hole, can localize in the intralayer space that does not contain water in the Ca rich samples and in the interlayer regions without Ca in the low Ca content samples. The hole can contribute to H_2 production in this latter case.

This mechanism, although efficient in terms of H_2 production, was shown to be hindered by the presence of calcite, portlandite and quartz in cement paste. Furthermore, in these cases, the level of H_2 production is negligible when the cement paste is dried, meaning that H_2 accumulation will not be a problem as long as the relative humidity of the containers is maintained at a low level. H_2 production however drastically increases with increasing relative humidity, which can be a concern in the context of nuclear waste storage as it will be difficult, if not impossible, to maintain a low relative humidity in the storage facilities over long periods of time. The so-called “nuclear cement”, which has a silica-enriched composition with a 10% mass percentage of ettringite and portlandite proved to have the best resistance regarding H_2 production over time. The use of quartz-enriched cement formulations is consequently of interest to delay H_2 accumulation in nuclear waste storage facilities since the interactions between containers and the host humid geological media will lead to increasing levels of relative humidity in cement paste over time.

Acknowledgments

The NEEDS MIPOR and NEEDS Déchets programs as well as the Schlumberger-MIT cement research collaboration X-Cem are gratefully acknowledged for financial support. Computer time on ARCHER, the UK national Supercomputing Service, was provided by the UK Car-Parrinello

Consortium through EPSRC grant EP-K013459/1. Dr Pascal Bouniol is gratefully acknowledged for fruitful discussions.

Supplementary data. Supplementary data to this article are available.

References

[1] D. Butler, Call for better oversight of nuclear waste storage, Nature 509 (2014) 267-268.
[2] P.C. Burns, R.C. Ewing, A. Navrotsky, Nuclear Fuel in a Reactor Accident, Science 335 (2012) 1184-1188.
[3] N. Kinoshita, K. Sueki, K. Sasa, J.-I. Kitagawa, S. Ikarashi, T. Nishimura, Y.-S. Wong, Y. Satou, K. Handa, T. Takahashi, M. Sato, T. Yamagata, Assessment of individual radionuclide distributions from the Fukushima nuclear accident covering central-east Japan, Proc. Natl. Acad. Sci. USA 108 (2011) 19526-19529.
[4] L.R. Anspaugh, R.J. Catlin, M. Goldman, The global impact of the Chernobyl reactor accident, Science 242 (1988) 1513-1519.
[5] T.J. Yasunari, A. Stohl, R.S. Hayano, J.F. Burkhart, S. Eckhardt, T. Yasunari, Cesium-137 deposition and contamination of Japanese soils due to the Fukushima nuclear accident, Proc. Natl. Acad. Sci. USA 108 (2011) 19530-19534.
[6] A.J. Allen, J.J. Thomas, H.M. Jennings, Composition and Density of Nanoscale Calcium–Silicate–Hydrate in Cement, Nature Mat. 2007 (2007) 311-316.
[7] R.J.-M. Pellenq, A. Kushima, R. Shahsavari, K.J. Van Vliet, M.J. Buehler, S. Yip, F.-J. Ulm, A realistic molecular model of cement hydrates, Proc. Natl. Acad. Sci. USA 106 (2009) 16102-16107.
[8] H.M. Jennings, Refinements to Colloid Model of C-S-H in Cement: CM-II, Cement Concrete Res. 38 (2008) 275-289.
[9] P.J. McDonald, J.-P. Korb, J. Mitchell, L. Monteilhet, Surface relaxation and chemical exchange in hydrating cement pastes: A two-dimensional NMR relaxation study, Phys. Rev. E 72 (2005) 011409.
[10] P.J. McDonald, V. Rodin, A. Valori, Characterisation of intra- and inter-C–S–H gel pore water in white cement based on an analysis of NMR signal amplitudes as a function of water content, Cem. Concr. Res. 40 (2010) 1656-1663.
[11] A.C.A. Muller, K.L. Scrivener, A.M.M. Gajewicz, P.J., Densification of C-S-H measured by H NMR relaxometry J. Phys. Chem. C 117 (2013) 403-412.
[12] J.W.T. Spinks, R.J. Woods, *An Introduction to Radiation Chemistry*. 3rd ed, Wiley-Interscience Publication: New York, USA, 1990.
[13] R.C. Ewing, W.J. Weber, F.W. Clinard Jr, Radiation effects in nuclear waste forms for high-level radioactive waste, Prog. Nucl. Energy 29 (1995) 63-127.
[14] N. Mobasher, S.A. Bernal, H. Kinoshita, C.A. Sharrad, J.L. Provis, Gamma irradiation resistance of an early age slag-blended cement matrix for nuclear waste encapsulation, J. Mat. Res. 30 (2015) 1563-1571.
[15] T.M. Rosseel, I. Maruyama, Y. Le Pape, O. Kontani, A.B. Giorla, I. Remec, J.J. Wall, M. Sircar, C. Andrade, M. Ordonez, Review of the Current State of Knowledge on the Effects of Radiation on Concrete, J. Adv. Concrete Technol. 14 (2016) 368-383.
[16] P. Bouniol, E. Bjergbakke, A comprehensive model to describe radiolytic processes in cement medium, J. Nucl. Mat. 372 (2008) 1-15.
[17] L. Dezerald, J.J. Kohanoff, A.A. Correa, A. Caro, R.J.-M. Pellenq, F.-J. Ulm, A. Saul, Cement As a Waste Form for Nuclear Fission Products: The Case of 90Sr and Its Daughters, Environ. Sci. Technol. 49 (2015) 13676-13683.
[18] S. Le Caër, P. Rotureau, F. Brunet, T. Charpentier, G. Blain, J.P. Renault, J.-C. Mialocq, Radiolysis of Confined Water: Hydrogen Production at a High Dose Rate, ChemPhysChem 6 (2005) 2585-2596.

[19] N. Brodie-Linder, S. Le Caër, M.S. Alam, J.P. Renault, C. Alba-Simionesco, H_2 Formation by Electron Irradiation of SBA-15 Materials and the Effect of Cu^{II} Grafting, Phys. Chem. Chem. Phys. 12 (2010) 14188-14195.
[20] S. Le Caër, Water radiolysis: influence of oxide surfaces on H2 production under ionizing radiation, Water 3 (2011) 235-253.
[21] J.K. Thomas, Physical Aspects of Photochemistry and Radiation Chemistry of Molecules Adsorbed on SiO_2, gamma-Al_2O_3, Zeolites, and Clays., Chem. Rev. 93 (1993) 301-320.
[22] C. Fourdrin, H. Aarrachi, C. Latrille, S. Esnouf, F. Bergaya, S. Le Caër, Water radiolysis in exchanged-montmorillonites: the H2 production mechanisms, Environ. Sci. Technol. 47 (2013) 9530-9537.
[23] M. Lainé, E.A. Balan, Th. , F. Martin, H.-J. von Bardeleben, J.-L. Robert, S. Le Caër, Reaction mechanisms in talc under ionizing radiation: evidence of a high stability of $H^{\bullet}$ atoms, J. Phys. Chem. C 120 (2016) 2087-2095.
[24] M. Lainé, E. Balan, T. Allard, E. Paineau, P.M. Jeunesse, M., J.-L. Robert, S. Le Caër, Reaction mechanisms in swelling clays under ionizing radiation: influence of the water amount and of the nature of the clay mineral, RSC Adv. 526 (2017) 526-534.
[25] D. Sassani, E. Hardin, DOE Deep Borehole Field Test: Site Characterization and Design Requirements, International Technical Workshop on Deep Borehole Disposal of Radioactive Waste U.S. Nuclear Waste Technical Review Board, Washington D.C. (2015) October 20-21.
[26] E. Hardin, Deep Borehole Field Test Waste Packaging, Emplacement and Seals Testing, U.S. Nuclear Waste Technical Review Board Visit Albuquerque, NM (2015) July 16.
[27] P.K. Mehta, P.J.M. Monteiro, *Concrete: Microstructure, Properties, and Materials* 3rd edition ed, McGraw-Hill, 2006.
[28] E.B. Nelson, D. Guillot, *Well Cementing*. second edition ed, Schlumberger, 2006.
[29] H. Taylor, *Cement Chemistry*, ed. T. Telford, 1997.
[30] K.J. Krakowiak, J.J. Thomas, S. Musso, S. James, A.-T. Akono, F.-J. Ulm, Nano-chemo-mechanical Signature of Conventional Oil-Well Cement Systems: Effects of Elevated Temperature and Curing Time, Cement Concrete Res. 67 (2015) 103-121.
[31] R.A. Cook, K.C. Hover, Mercury porosimetry of hardened cement pastes, Cem. Concr. Res. 29 (1999) 933-943.
[32] C. Cau-dit-Coumes, *Alternative Binders to Ordinary Portland Cement for Radwaste Solidification and Stabilization*, in *Cement-Based Materials for Nuclear Waste Storage*, F. Bart, C. Cau-dit-Coumes, F. Frizon, and S. Lorente, Editors. 2013, Springer: New York. p. 171-191.
[33] P. Faucon, F. Adenot, J.-F. Jacquinot, J.-C. Petit, R. Cabrillac, M. Jorda, Long-Term Behaviour of Cement Pastes Used for Nuclear Waste Disposal: Review of Physico-Chemical Mechanisms of Water Degradation, Cem. Concr. Res. 28 (1998) 847-857.
[34] Y. Suda, T. Saeki, T. Saito, Relation between Chemical Composition and Physical Properties of C-S-H Generated from Cementitious Materials, J. Adv. Concrete Technol. 13 (2015) 275-290.
[35] H.F.W. Taylor, Bound Water in Cement Pastes and its Significance for Pore Solution Compositions, MRS Proc. 85 (1986) 47-54.
[36] S.M. Antao, M.J. Duane, I. Hassan, DTA, TG, and XRD Studies of Sturmanite and Ettringite, Canadian Mineralogist 40 (2002) 1403-1409.
[37] B. Lothenbach, P. Durdzinski, K. De Weerdt, *Thermogravimetric analysis*, in *A Practical Guide to Microstructural Analysis of Cementitious Materials*. 2016, CRC Press: Boca Raton. p. 177-211.
[38] V. Rostami, Y. Shao, A.J. Boyd, Z. He, Microstructure of cement paste subject to early carbonation curing, Cement Concrete Res. 42 (2012) 186-193.
[39] J.C. Mialocq, B. Hickel, G. Baldacchino, M. Juillard, The radiolysis project of CEA, J. Chim. Phys. 96 (1999) 35-43.
[40] H. Fricke, J.E. Hart, *Chemical Dosimetry*, in *Radiation Dosimetry*, F.H. Attix and W.C. Roesch, Editors. 1966, Academic press: New York and London. p. 167-232.

[41] S. Merlino, E. Bonaccorsi, T. Armbruster, The Real Structure of Tobermorite 11 A: Normal and Anomalous Forms, OD Character and Polytypic Modifications, Eur. J. Mineral. 13 (2001) 577-590.
[42] J. Hutter, M. Iannuzzi, F. Schiffmann, J. VandeVondele, CP2K: atomistic simulations of condensed matter systems, WIREs Comput. Mol. Sci. 4 (2014) 15-25.
[43] G. Lippert, J. Hutter, M. Parrinello, A hybrid Gaussian and plane wave density functional scheme, Mol. Phys. 92 (1997) 477-488.
[44] J. VandeVondele, M. Krack, F. Mohamed, M. Parrinello, T. Chassaing, J. Hutter, Quickstep: Fast and accurate density functional calculations using a mixed Gaussian and plane wave approach, Comput. Phys. Commun. 167 (2005) 103-128.
[45] J. VandeVondele, J. Hutter, Gaussian basis sets for accurate calculations on molecular systems in gas and condensed phases, J. Chem. Phys. 127 (2007) 114105.
[46] Y. Zhao, D.G. Truhlar, The M06 suite of density functionals for main group thermochemistry, thermo-chemical kinetics, noncovalent interactions, excited states, and transition elements: two new functionals and systematic testing of four M06-class functionals and 12 other functionals, Theor. Chem. Account 120 (2008) 215-241.
[47] J.P. Perdew, K. Burke, M. Ernzerhof, Generalized Gradient Approximation Made Simple, Phys. Rev. Lett. 77 (1996) 3865-3868.
[48] S. Goedecker, M.H. Teter, J., Separable dual-space Gaussian pseudopotentials, Phys. Rev. B 54 (1996) 1703-1710.
[49] C. Hartwigsen, S. Goedecker, J. Hutter, Relativistic separable dual-space Gaussian pseudo-potentials from H to Rn, Phys. Rev. B 58 (1998) 3641-3662.
[50] S. Grimme, J. Antony, S. Ehrlich, H. Krieg, A consistent and accurate ab initio parametrization of density functional dispersion correction (DFT-D) for the 94 elements H-Pu, J. Chem. Phys. 132 (2010) 154104.
[51] S. Grimme, S. Ehrlich, L. Goerigk, Effect of the damping function in dispersion corrected density functional theory, J. Comput. Chem. 32 (2011) 1456-1465.
[52] O. Gunnarsson, B.I. Lundqvist, Exchange and correlation in atoms, molecules, and solids by the spin-density-functional formalism, Phys. Rev. B 13 (1976) 4274-4298.
[53] M. Guidon, F. Schiffmann, J. Hutter, J. VandeVondele, Ab initio molecular dynamics using hybrid density functionals, J. Chem. Phys. 128 (2008) 214104.
[54] M. Guidon, J. Hutter, J. VandeVondele, Robust Periodic Hartree-Fock Exchange for Large-Scale Simulations Using Gaussian Basis Sets, J. Chem. Theory Comput. 5 (2009) 3010-3021.
[55] M. Guidon, J. Hutter, J. VandeVondele, Auxiliary Density Matrix Methods for Hartree-Fock Exchange Calculations, J. Chem. Theory Comput. 6 (2010) 2348-2364.
[56] P.B. Giannozzi, S. Bonini, N., M. Calandra, R. Car, C. Cavazzoni, D. Ceresoli, G.L. Chiarotti, M. Cococciono, I. Dabo, A.D. Corso, S. de Gironcoli, S. Fabris, G. Fratesi, R. Gebauer, U. Gerstmann, C. Gougoussis, A. Kokalj, M. Lazzeri, L. Martin-Samos, N. Marzari, F. Mauri, R. Mazzarello, S. Paolini, A. Pasquarello, L. Paulatto, C. Sbraccia, S. Scandolo, G. Sclauzero, A.P. Seitsonen, A. Smogunov, P. Umari, R.M. Wentzcovitch, QUANTUM ESPRESSO: a modular and open-source software project for quantum simulations of materials, J. Phys.: Condens. Matter 21 (2009) 395502.
[57] G. Bussi, D. Donadio, M. Parrinello, Canonical sampling through velocity rescaling, J. Chem. Phys. 126 (2007) 014101.
[58] J. Kolafa, Time-reversible always stable predictor-corrector method for molecular dynamics of polarizable molecules, J. Comput. Chem. 25 (2004) 335-342.
[59] D. Russell, P.A.M. Basheer, G.I.B. Rankin, A.E. Long, Effect of relative humidity and air permeability on prediction of the rate of carbonation of concrete Proceed. Institut. Civil Engin.. Struct. Buildings 146 (2001) 319-326.
[60] L.G. Baquerizo, T. Matschei, K.L. Scrivener, M. Saeidpour, L. Wadsö, Hydration states of AFm cement phases, Cem. Concr. Res. 73 (2015) 143-157.
[61] A. Morandeau, M. Thiéry, P. Dangla, Investigation of the carbonation mechanism of CH and C-S-H in terms of kinetics, microstructure changes and moisture properties, Cem. Concr. Res. 56 (2014) 153-170.

[62] J. Cunningham, Electron-Hole Trapping in X-Irradiated Calcium Carbonate and Sodium Nitrate, J. Phys. Chem. 71 (1967) 1967-1970.
[63] P. Bouniol, S. Lapuerta-Cochet, The solubility product of calcium peroxide octahydrate in relation to temperature; its influence on radiolysis in cement-based materials, J. Nucl. Mater. 420 (2012) 16-22.
[64] J.A. LaVerne, L. Tandon, H_2 and Cl_2 Production in the Radiolysis of Calcium and Magnesium Chlorides and Hydroxides, J. Phys. Chem. A 109 (2005) 2861-2865.
[65] J.A. Weil, A review of electron spin spectroscopy and its application to the study of paramagnetic defects in crystalline quartz, Phys. Chem. Minerals 10 (1984) 149-165.
[66] L. Frances, M. Grivet, J.P. Renault, J.-E. Groetz, D. Ducret, Hydrogen radiolytic release from zeolite 4A/water systems under γ irradiations, Rad. Phys. Chem. 110 (2015) 6-11.
[67] C.M. Biagioni, S., E. Bonaccorsi, The Tobermorite Supergroup: A New Nomenclature, Mineral. Mag. 79 (2015) 485-495.

TOC FIGURE

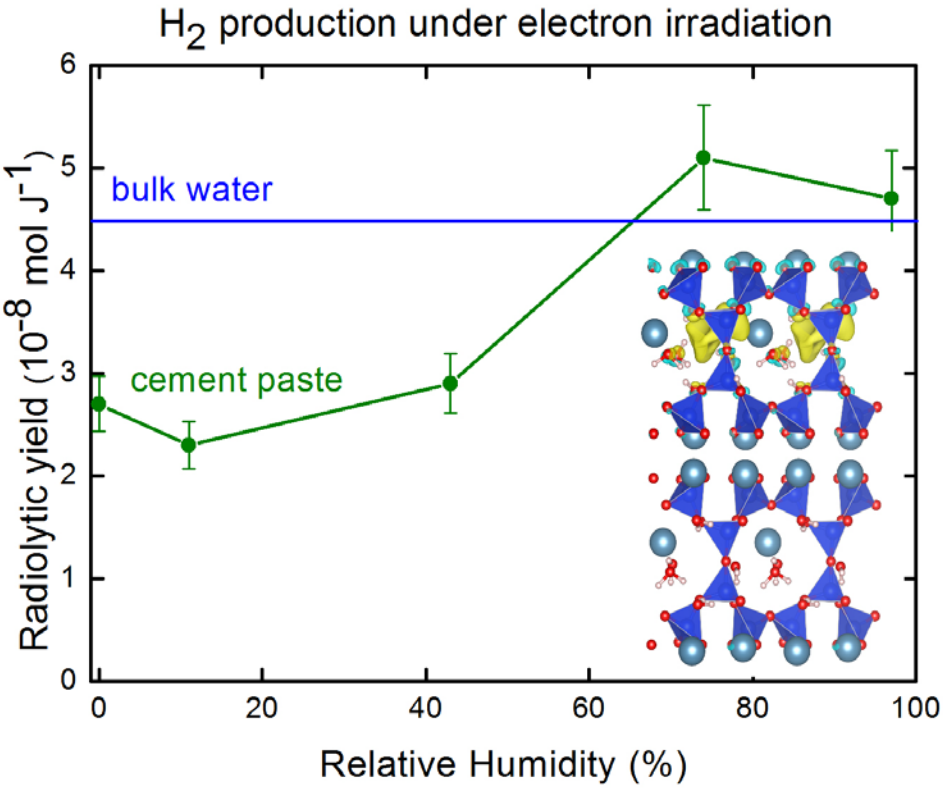
H2 production under electron irradiation
Radiolytic yield (10-8 mol J-1)
Relative Humidity (%)
bulk water
cement paste
0
1
2
3
4
5
6
0
20
40
60
80
100

Supporting Information for "Production of H_2 by water radiolysis in cement paste under electron irradiation: a joint experimental and theoretical study"

Sophie Le Caër[a*], Lucile Dezerald[b,c,d], Khaoula Boukari[e], Maxime Lainé[a], Sébastien Taupin[a,b,c3], Ryan M. Kavanagh[f], Conrad S. N. Johnston[f], Eddy Foy[a], Thibault Charpentier[a], Konrad J. Krakowiak[g,,b], Roland J.-M. Pellenq[b,c,e], Franz J. Ulm[b,c], Gareth A. Tribello[f], Jorge Kohanoff[f], and Andres Saúl[e*]

[a]*NIMBE UMR 3685, CEA, CNRS, Université Paris Saclay, CEA Saclay, F-91191 Gif-sur-Yvette Cedex, France*

[b]*Department of Civil and Environmental Engineering, Massachusetts Institute of Technology, Cambridge, Massachusetts 02139, United States*

[c]*MultiScale Material Science for Energy and Environment, UMI 3466 CNRS-MIT, 77 Massachusetts Avenue, Cambridge, Massachusetts 02139, United States*

[d]*Institut Jean Lamour, Université de Lorraine - CNRS, F-54011 Nancy, France*

[e]*Aix-Marseille University, CINaM-CNRS UMR 7325 Campus de Luminy, 13288 Marseille cedex 9, France*

[f]*Atomistic Simulation Centre, Queen's University Belfast, University Road, Belfast BT9 1NN, UK*

[g]*Department of Civil and Environmental Engineering, Cullen College of Engineering, University of Houston, Houston, Texas 77204-4003, United States*

**Corresponding authors: sophie.le-caer@cea.fr; saul@cinam.univ-mrs.fr*

Supporting Information 1 – Pore size distribution in sample S3 measured with Mercury Intrusion Porosimetry (MIP)

Mercury intrusion porosimetry (MIP) was used to characterize the medium and large capillary porosity, as well as the pore size distribution, using an AutoPore IV 9500 instrument (Micromeritics, US). The intrusion pressure ranged from 3.5×10^{-3} MPa to 228 MPa, discretized into 70 pressure steps equally spaced on a logarithmic scale, equilibration time 15 sec., evacuation pressure 50 μm Hg, and mercury filling pressure 3.5×10^{-3} MPa. A value of 140 degrees was assumed for the contact angle, and 0.48 N m^{-1} for the surface tension of mercury. Cement paste samples, with mass of around 0.6 g, were dried by solvent exchange (isopropanol) followed by oven drying to a constant mass at 50°C. Two samples per specimen were analyzed, and the reproducibility of the measurements was very good.

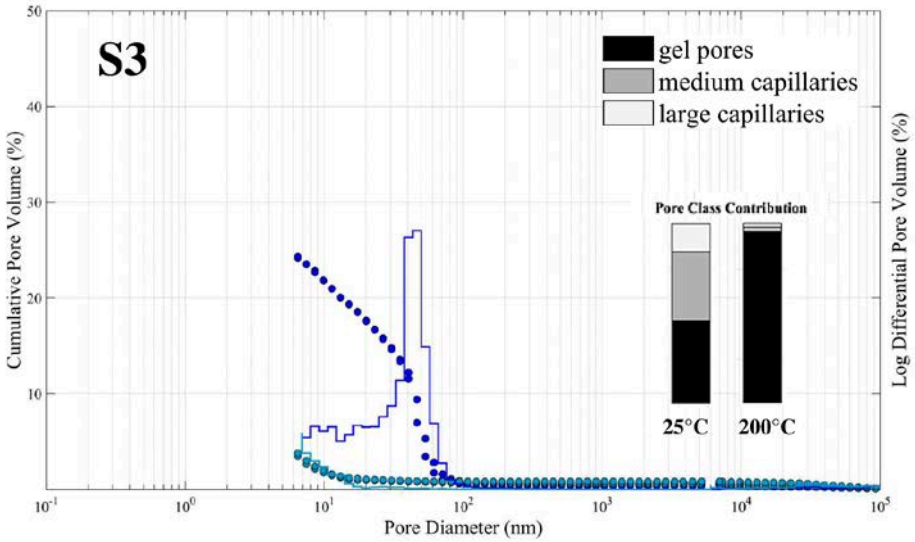

Figure SI1-1. Pore size distribution of the sample S3 before (dark blue) and after (light blue) hydrothermal exposure measured with mercury intrusion (MIP). Pore classification after ref. [1].

Noteworthy, in general, the amount of the capillary porosity in the hydrated cement paste is determined by the water-to-cement ratio. Thus, higher capillary and total porosity is expected in the cement pastes with the higher initial water content as originally described by the Powers-Brownyard model [2], and experimentally measured e.g. [3] (case of samples S1 and S2). On the other hand, pozzolanic reaction results in the additional fraction of low-calcium C-S-H gel, which effectively fills the void space and shifts the pores size distribution toward the gel porosity fraction [2, 4] as evidenced here in the case of S3.

Supporting Information 2 – X-ray Diffration (XRD) data

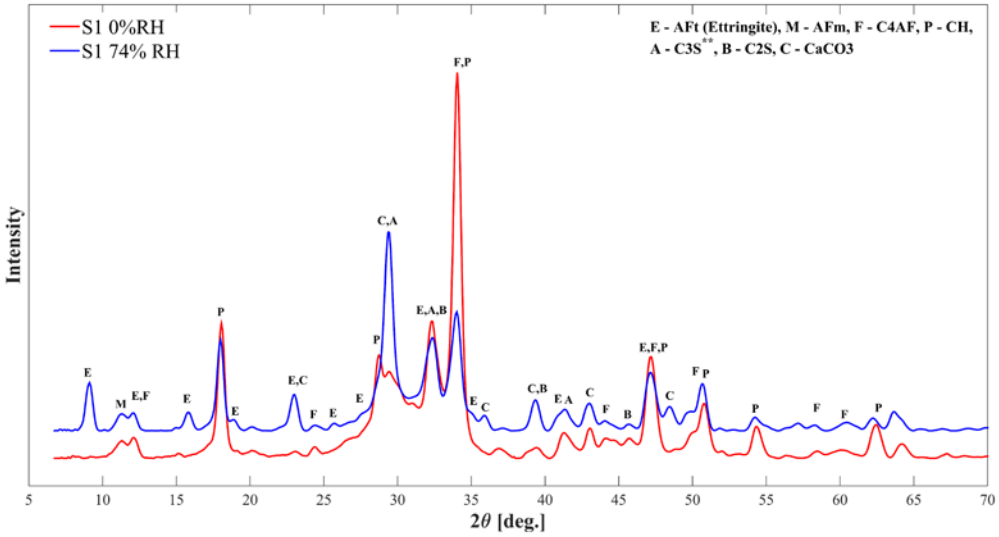

Figure SI2-1. Qualitative analysis of the X-ray (Cu $K\alpha_1$=1.540598 Å) powder diffraction results obtained on S1 hydrated cement paste equilibrated at 0% RH (red) and 74% RH (blue). Samples aged 28 days. To make the comparison with literature data easier, the diagrams, recorded with a molybdenum anode ($\lambda K_{\alpha 1}$ = 0.70932 Å), were then calculated with respect to a copper anode ($\lambda K_{\alpha 1}$ = 1.540598 Å).

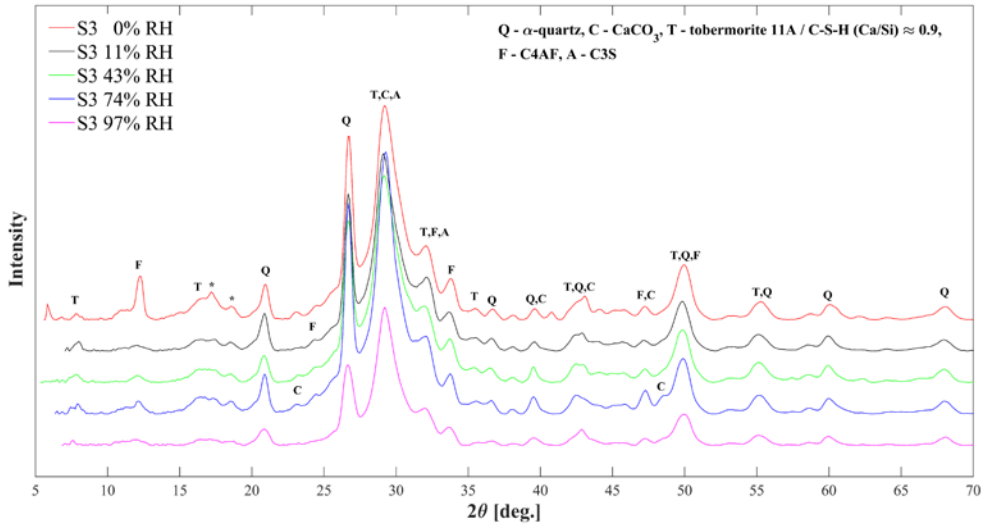

Figure SI2-2. Qualitative analysis of the X-ray (Cu $K\alpha_1$=1.540598 Å) powder diffraction results obtained on S3 hydrated cement paste with silica enrichment (C-S-H matrix with the approximate Ca/Si ≈ 0.92) equilibrated at 0, 11, 43, 74 and 97% RH. To make the comparison with literature data easier, the diagrams, recorded with a molybdenum anode ($\lambda K_{\alpha 1}$ = 0.70932 Å), were then calculated with respect to a copper anode ($\lambda K_{\alpha 1}$ = 1.540598 Å). * - unidentified peaks in the proximity of 101 reflection of ordered 11Å tobermorite, also typical of nano-crystalline disordered tobermorite structure [5, 6], T – diffraction lines due to crystalline and semi-crystalline calcium silicate hydrates, 11Å tobermorite and C-S-H.

The diffraction patterns of S2 are not presented as they are very similar to S1 with the exception that α-quartz peaks are present in the spectra (S2 mix includes 28% wt. of quartz, 47% wt. of cement and 25% wt. of water.

The identification of the different phases found by XRD in all samples is summarized in Table SI2-1. Dry samples S1 and S2 contain AFm. At higher relative humidities, ettringite is also present, as evidenced in Figure SI2-1.

Sample	**Phases identified**
S1	Portlandite (CH) (PDF 044-1481), Calcite (PDF 005-0586), Ettringite (AFt) (PDF 041-1451), Tricalcium monosulpho-aluminate (AFm) [2], Alite (C_3S) [2], Belite (C_2S) [2], Ferrite (Brownmillerite, C4AF) (PDF 030-0226)
S2	Same as S1 + α-quartz (PDF 046-1045)
S3	α-quartz (PDF 046-1045), Calcite (PDF 005-0586), Tobermorite (PDF 45-1480), Ferrite (Brownmillerite, PDF 030-0226), Alite [2]

Table SI2-1. Identification of the different phases determined by XRD. In S1 and S2, ettringite is not present at the lowest relative humidity.

Supporting Information 3 – Infrared (IR) spectroscopy

Infrared (IR) spectra were recorded in transmission mode in the 4000-370 cm^{-1} energy range with a Bruker Tensor 27 FT-IR spectrophotometer. 1% of sample was pelletized in KBr. All the spectra were collected with a 4 cm^{-1} resolution from 100 scans. The data were analyzed using the OPUS software. The background (KBr pellet) was subtracted in all cases. The IR spectra recorded for all samples are given in Figure SI3-1.

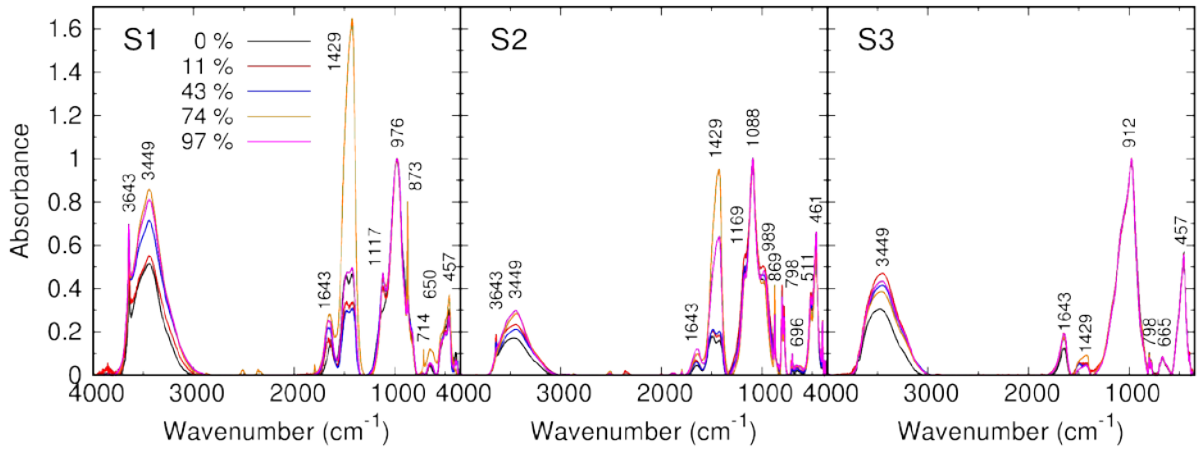

Figure SI3-1. Infrared spectra for all samples. The spectra are normalized with respect to the band around 970-1100 cm^{-1}, which corresponds to Si-O stretching vibrations.

At the highest wavenumbers, a very acute peak is detected at 3643 cm^{-1} in the O-H stretching region. It corresponds to the stretching mode of O-H in portlandite. This band is not detectable in the S3 sample for which the portlandite is not present (Figure SI3-1). A broad band is observed between 3500 cm^{-1} and 3100 cm^{-1} (with a maximum around 3449 cm^{-1}) that corresponds to the O-H stretching mode of adsorbed water molecules. The width of the band for the O-H stretching mode illustrates the variety of H bonds that are found in cement paste: the strongest H bonds lead to the lowest wavenumbers, and the weakest H bonds lead to the highest wavenumbers [7]. Consequently, the broader the peak, the larger variety in H-bonds strength is present in our sample. One can see that the larger the relative humidity, the higher and broader the peak, as expected, which is consistent with the fact that the evaporable water content increases with relative humidity (Figure 1b in the main text). This constitutes the largest variations observed in all samples. In all cases (except the S1 sample), the maximum of the band is shifted towards lower wavenumbers when the relative humidity increases, as expected (from roughly 3470-3480 cm^{-1} at 0% RH to 3440-3450 cm^{-1} at 97% RH). The shift to lower wavenumbers corresponds to a strengthening of the H bond. This slight decrease may suggest that water fills larger pores when RH is increasing which is consistent with the swelling character of these systems. Nevertheless, in the case of the S1 sample, the maximum of the band is not very sensitive to the relative humidity and remains around 3440 cm^{-1}.

The band detected at 1643 cm^{-1} corresponds to the H-O-H bending mode of adsorbed water molecules [7]. The main bands correspond either to CO_3^{2-} modes (which are clearly seen when calcite is present, see for example the band at 1429 cm^{-1} for S1 and S2, especially at 74% RH) and are described in the tables below [8, 9]. The maximum of the Si-O stretching band is at 970-980 cm^{-1}, as expected in the case of C-S-H for S1 and S3 samples [8]. It is shifted to 1090 cm^{-1} in the case of S2 due to the presence of quartz [10]. The presence of quartz in S3 is also observed around 1090 cm^{-1} as a shoulder, indicating that the quartz content is much smaller than in S2. The infrared spectra enable the identification of some phases present in the samples (Table SI3-2).

Wavenumber (cm^{-1})	Assignment
3643	O-H stretching of $Ca(OH)_2$
3500 - 3100	O-H stretching mode of adsorbed water molecules
1643	bending of water molecules
1429	asymmetric stretching CO_3^{2-} (calcite)
1100-1200	stretching of sulfates
950-1200	asymmetric and symmetric stretching vibrations of Si-O bonds
870-875	Out-of-plane bending of CO_3^{2-} (calcite)
714	stretching of CO_3^{2-} (calcite)
650	Si-O-Si bending vibrations
457	deformation of SiO_4 tetrahedra

Table SI3-1. IR wavenumbers of the main IR bands detected [8, 9].

Wavenumber (cm^{-1})	Nature of the phase
3643	portlandite
1429/870-875/714	calcite
1100-1200	ettringite/AFm
~ 1090	quartz

Table SI3-2. Link between the detected wavenumbers and the nature of the present phases

Supporting Information 4 – Thermogravimetric Analysis (TGA)

Thermogravimetric Analysis (TGA) – Differential ThermoGravimetry (DTG) measurements enabled performing quantitative analysis of the samples composition for ettringite, portlandite, calcite, as well as quantifying the amount of water (evaporable and chemically bond). Other phases such as AFm and C-S-H could not be quantified with this technique since the corresponding weight loss happens in the same temperature range (around 150-200˚C) and cannot be distinguished from one another. The results obtained for sample S2 at 11% RH are given in Fig. SI4-1 and details on interpretation is given below.

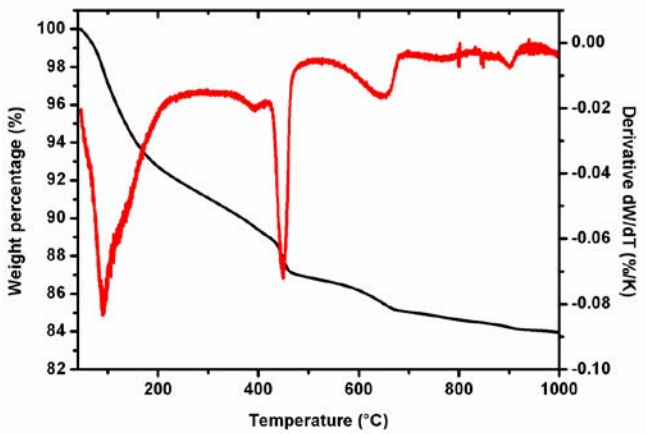

Figure SI4-1. TGA (in black) and the differential curve (DTG, in red) curves of S2 at 11% RH.

As stated in reference [11], we consider that the weight loss between ambient temperature and 105°C corresponds to the loss of evaporable water (EW). In some cases, around 110°C, an additional loss of water molecules is due to the presence of ettringite (Figure SI4-1). The ideal formula of ettringite is $3\,CaO{\bullet}Al_2O_3{\bullet}3\,CaSO_4{\bullet}32\,H_2O$ (1255.1 $g.mol^{-1}$) and, as stated in reference [12], the TGA loss corresponds to the release of roughly 27 water molecules. Hence, an approximate percentage of ettringite in the sample is given by the mass percentage difference of the additional mass loss multiplied by the ratio of the molar mass of ettringite (1255.1 $g.mol^{-1}$) and of 27 water molecules (486.3 $g.mol^{-1}$), which is equal to 2.58.

The DTG peak between 410 and 500°C corresponds to the loss of free portlandite ($Ca(OH)_2$, labeled CH) and is calculated as follows [4]:

$$Ca(OH)_2 \rightarrow CaO + H_2O$$

The amount of free CH corresponds then to the mass percentage difference at the two temperatures multiplied by the ratio of the molar mass of $Ca(OH)_2$ (74.09 $g.mol^{-1}$) and of H_2O (18.01 $g.mol^{-1}$), which is equal to 4.11.

The DTG peak between 550°C and 800°C is assigned to the decarbonation of calcite $CaCO_3$ according to the following reaction:

$$CaCO_3 \rightarrow CaO + CO_2$$

The amount of calcite corresponds to the mass percentage difference at the two temperatures multiplied by the ratio of the molar mass of $CaCO_3$ (100.09 $g.mol^{-1}$) and of CO_2 (44.01 $g.mol^{-1}$), which is equal to 2.27.

The chemically bound water (CBW) is then calculated as the weight loss between 105°C (corresponding to evaporable water, see above) and the highest temperature (1000°C), minus the weight loss due to decarbonation of calcite. It thus contains the –OH groups of portlandite for instance, and, more generally, –OH groups and chemically bound water molecules.

Supporting Information 5 – ^{29}Si Nuclear Magnetic Resonance (NMR)

^{29}Si MAS NMR spectra were collected on a Bruker DMX 300 spectrometer (operating at a magnetic field of 7.02T) using a Bruker Cross-Polarization – Magic Angle Spinning (CP-MAS) probe. The MAS experiment removes broadening effects of anisotropic couplings (such as dipolar couplings with the other nuclei and chemical shift anisotropy). The samples were kept after irradiation in ampoules under argon atmosphere to prevent atmospheric CO_2 contamination. Powdered samples of about 300 mg were introduced in 7 mm outside diameter (o.d.) ZrO_2 rotors. To allow comparison between different NMR spectra, the mass of each sample was carefully weighed. For each sample, ^{1}H - ^{29}Si CP-MAS and ^{29}Si MAS spectra were acquired on the spectrometer for a total accumulation time of approximatively 23 hours using a recycle delay of 120 s. Each ^{29}Si MAS NMR spectrum was analyzed using Gaussian/Lorentzian lineshapes with a home-made program. The model is detailed in references [13, 14].

The silicate tetrahedra are usually referred to as Q^n where Q represents the SiO_4 tetrahedron and *n* is the number of other tetrahedra to which it is linked. Q^n sites are spread in the -60 ppm to -120 ppm range as presented in Figures SI5-2-4. The chemical shift decreases when *n* increases [15].

The ^{29}Si MAS NMR spectra of samples at 11% RH are given in Figures SI5-2 to SI5-4. In all cases, the spectra are composed of three major peaks that are described in the following taking the example of S2 (Figure SI5-3) [16]. The first peak on the left of the spectra is located around -73 ppm, in the Q^0 range that corresponds to monomer silica tetrahedra. This narrow resonance is attributed to anhydrous phases (e.g. belite, alite) that remain after hydration of cement, as this peak disappears in the CP-MAS experiments. Then we observe a broad shape of unresolved resonances with peaks at about -78.0 ppm and -88.0 ppm which are attributed to Q^n unit tetrahedral (Q^1 and Q^2) of the calcium silicate hydrate (C-S-H) formed by hydration of the clinker. These peaks are visible for all the samples confirming the results obtained with FTIR and XRD experiments. Moreover, in S3, we observe components between roughly -90 and -100 ppm attributed to Q^3 sites. Finally the third peak at -108.1 ppm located on the right of Figures SI5-3-4 in the Q^4 range is noticed using ^{29}Si MAS NMR spectra (in black) but is absent with CP-MAS (in red) indicating that this peak is not protonated. This resonance is consequently due to quartz SiO_2. S2 and S3 are the only sample containing quartz as expected from the XRD results.

As shown in figure SI5-1 (left), quartz is characterized by a longitudinal relaxation time T1 longer than the recycle delay used (120 s) in contrast to other phases, for which spectra were found to give the same relative peak intensities. The analysis of the variation of the quartz peak intensity with the recycle delay (up to 1200 s) is displayed in figure SI5-1 (right), and gave an estimated value of T1 of 378 s using the following equation:

$$I(t_r) = I_\infty \left\{1 - \exp\left(-{}^{t_r}/_{T_1}\right)\right\}$$

Accordingly, the nominal population I_∞ of quartz can be estimated from the measurements $I(120s)$ using:

$$I_\infty = \frac{I(120s)}{\left\{1 - \exp\left(-\frac{120}{378}\right)\right\}} = 3.68 \times I(120s)$$

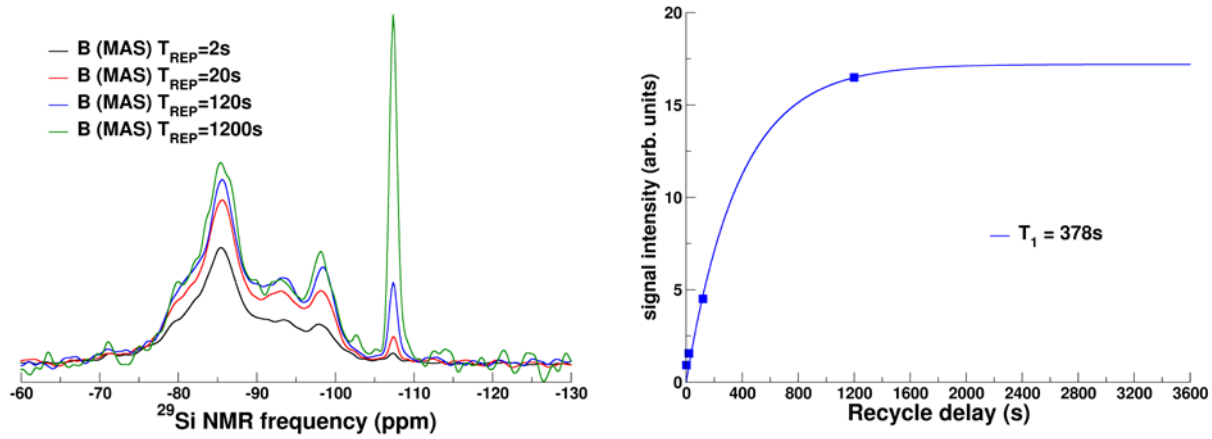

Figure SI5-1. (Left) Evolution of the ^{29}Si NMR spectra with the recycle delay for a sample similar to the ones studied in the present work. (Right) Intensity of the quartz peak (around -108 ppm) plotted as a function of the recycle delay.

From the three components deconvolution that fits properly the data, we can express the fraction of silicon atoms that belong to anhydrous phases (peak 1), C-S-H (peak 2) or quartz (peak 3) (see Table SI5-1, with values extracted from the recycle delay at 120 s).

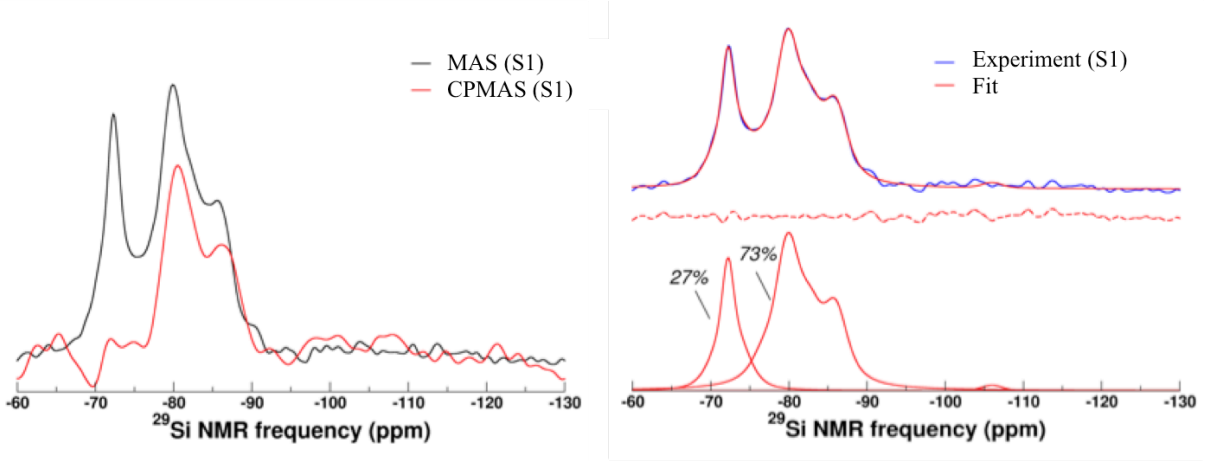

Figure SI5-2. Comparison between ^{29}Si MAS NMR and CP-MAS NMR spectra (left) of S1 equilibrated at 11% RH. Experimental (blue line) and simulated (red line) ^{29}Si MAS NMR spectra (right). The red dashed line represents the error.

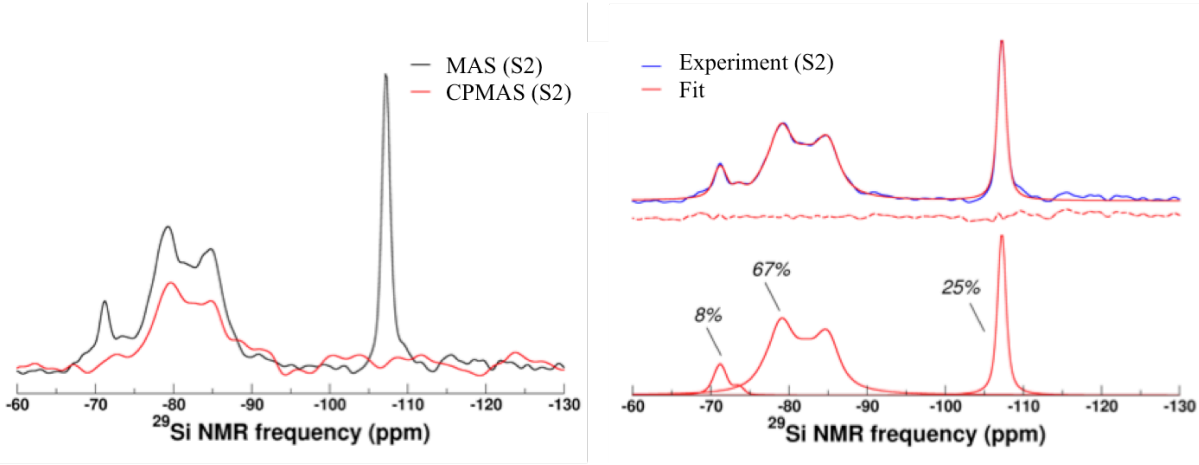

Figure SI5-3. Comparison between ^{29}Si MAS NMR and CP-MAS NMR spectra (left) for the S2 sample equilibrated at 11% RH. Experimental (blue line) and simulated (red line) ^{29}Si MAS NMR spectra (right). The red dashed line represents the error.

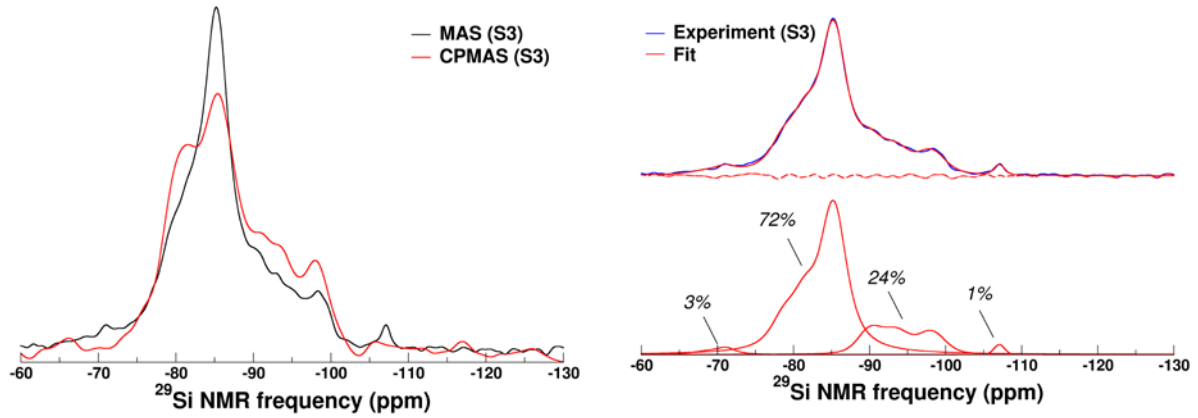

Figure SI5-4. Comparison between ^{29}Si MAS NMR and CP-MAS NMR spectra (left) for S3 equilibrated at 11% RH. Experimental (blue line) and simulated (red line) for the ^{29}Si MAS NMR spectra (right).

Samples	S1-11%	S2-11%	S3-11%
Anhydrous phases containing Si (%)	27	8	3
C-S-H (%)	73	67	96
Quartz (%)	0	25	1

Table SI5-1. Fraction of silicon atoms that belong to anhydrous phases containing silicon (alite, belite…), C-S-H and quartz. The values are extracted with a recycle delay of 120 s.

From this, we can get the correct fractions of each phase, by taking into account the relaxation effects, as explained above (Table SI5-2).

Samples	S1-11%	S2-11%	S3-11%
Anhydrous phases containing Si (%)	27	5	3
C-S-H (%)	73	40	93
Quartz (%)	0	55	4

Table SI5-2. Fraction of silicon atoms that belong to anhydrous phases containing silicon (alite, belite…), C-S-H and quartz, corrected from the relaxation effects.

Supporting Information 6 – Characterization of the samples before and after irradiation

The characterizations of S1 equilibrated at 11% RH before and after irradiation at 200 kGy are given in Figure SI6-1. No impact of ionizing radiation can be evidenced from these measurements. The results are the same for all samples, independently of the relative humidity.

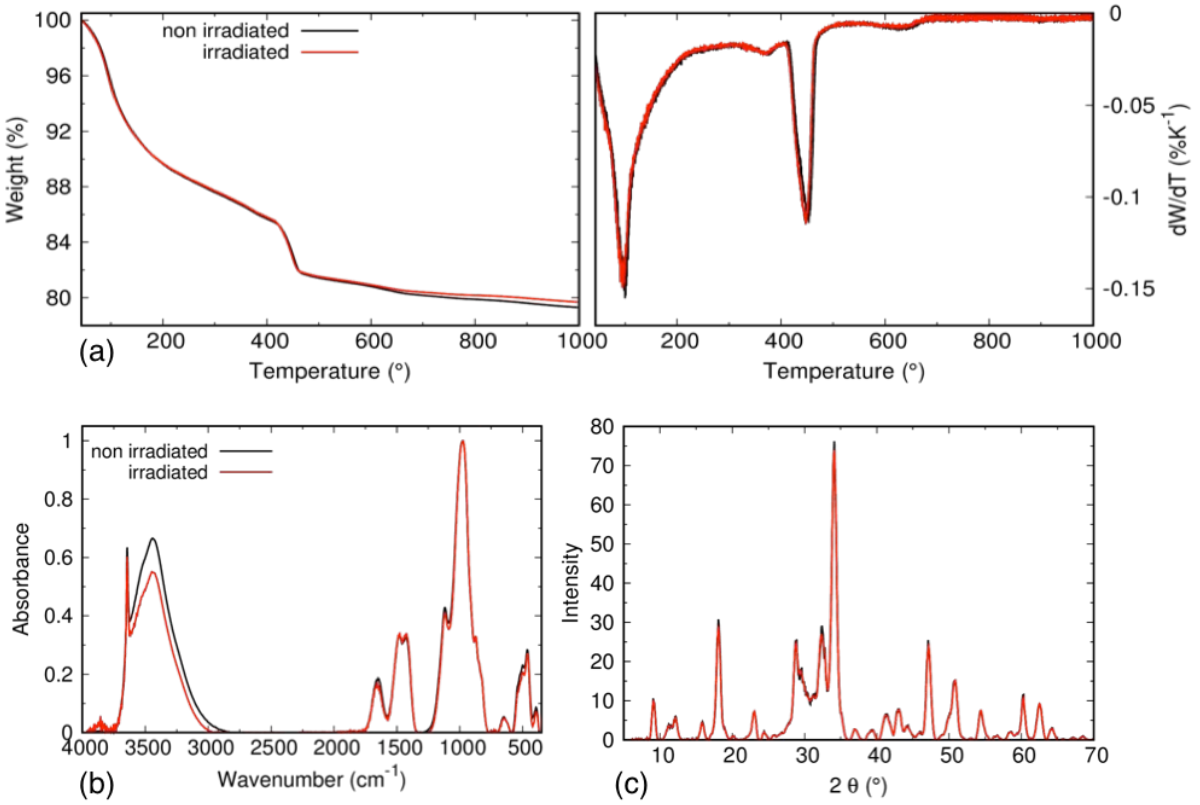

Figure SI6-1. S1 sample equilibrated at 11% RH before (in black) and after irradiation (red) at 200 kGy characterized by different techniques: a) TGA curves (left) and DTA curves (right); b) infrared spectroscopy and c) XRD analysis. Concerning the IR spectra, the discrepancy observed in the O-H stretching region (3000-4000 cm^{-1}) is due to the preparation of the pellets and is not significant.

Supporting Information 7 – Evolution of the H_2 radiolytic yield with the evaporable water content

To take into account the differences between the water amounts of the different samples, the dihydrogen radiolytic yield is represented in Figure SI7-1 as a function of the water amount. It is obvious from this figure that S3 has the highest H_2 yields, especially at the three lowest RH. In the case of S1 and S2, the decrease of the H_2 yield at 74% RH due to the high content of calcite is illustrated by two arrows in the figure. Globally, S1 and S2 exhibit the same trends. This proves that quartz has the same effects as the other H_2-inhibiting phases.

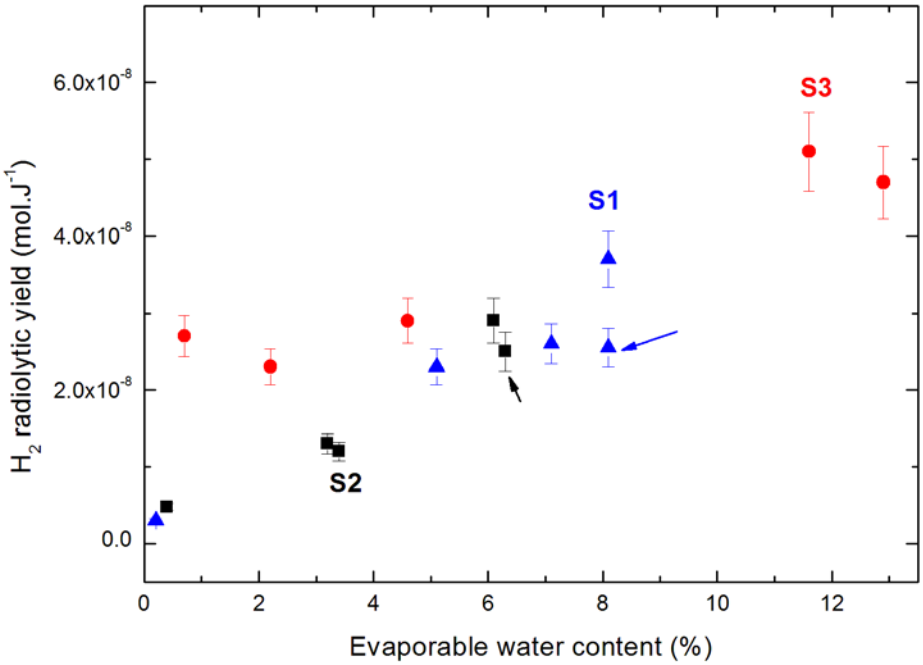

Figure SI7-1. Evolution of the H_2 radiolytic yield with the evaporable water content for S1 (blue triangles), S2 (black squares) and S3 (red circles). The arrows highlight the effect of the high calcite content for S1 and S2 at 74% RH.

References

[1] S. Mindess, J.F. Young, *Concrete*, Prentice-Hall: New Jersey, 1981.

[2] H. Taylor, *Cement Chemistry*, ed. T. Telford, 1997.

[3] R.A. Cook, K.C. Hover, Mercury porosimetry of hardened cement pastes, Cem. Concr. Res. 29 (1999) 933-943.

[4] K.J. Krakowiak, J.J. Thomas, S. Musso, S. James, A.-T. Akono, F.-J. Ulm, Nano-chemo-mechanical Signature of Conventional Oil-Well Cement Systems: Effects of Elevated Temperature and Curing Time, Cement Concrete Res. 67 (2015) 103-121.

[5] S. Grangeon, F. Claret, C. Lerouge, F. Warmont, T. Sato, S. Anraku, C. Numako, Y. Linard, B. Lanson, On the nature of structural disorder in calcium silicate hydrates with a calcium/silicon ratio similar to tobermorite, Cem. Concr. Res. 52 (2013) 31-37.

[6] S. Grangeon, F. Claret, Y. Linard, C. Chiaberge, X-ray diffraction: a powerful tool to probe and understand the structure on nanocrystalline calcium silicate hydrates, Acta Cryst. Section B 69 (2013) 465-473.

[7] S. Le Caër, S. Pin, S. Esnouf, Q. Raffy, J.P. Renault, J.-B. Brubach, G. Creff, P. Roy, A Trapped Water Network in Nanoporous Material: the Role of Interfaces, Phys. Chem. Chem. Phys. 13 (2011) 17658-17666.

[8] P. Yu, R.J. Kirkpatrick, B. Poe, P.F. McMillan, X. Cong, Structure of Calcium Silicate Hydrate (C-S-H): Near-, Mid-, and Far-Infrared Spectroscopy, J. Am. Ceram. Soc. 82 (1999) 742-748.

[9] R. Ylmen, U. Jäglid, B.-M. Steenari, I. Panas, Early Hydration and Setting of Portland Cement Monitored by IR, SEM and Vicat Techniques, Cement Concrete Res. 39 (2009) 433-439.

[10] N.B. Colthup, L.H. Daly, S.E. Wiberley, *Introduction to Infrared and Raman Spectroscopy, Third Edition*, Academic Press: San Diego, 1990.

[11] H.F.W. Taylor, Bound Water in Cement Pastes and its Significance for Pore Solution Compositions, MRS Proc. 85 (1986) 47-54.

[12] S.M. Antao, M.J. Duane, I. Hassan, DTA, TG, and XRD Studies of Sturmanite and Ettringite, Canadian Mineralogist 40 (2002) 1403-1409.

[13] F. Brunet, T. Charpentier, C.N. Chao, H. Peycelon, A. Nonat, Characterization by solid-state NMR and selective dissolution techniques of anhydrous and hydrated CEM V cement pastes, Cement Concrete Res. 40 (2010) 208-219.

[14] X. Pardal, F. Brunet, T. Charpentier, I. Pochard, A. Nonat, 27Al and 29Si Solid-State NMR Characterization of Calcium-Aluminosilicate-Hydrate, Inorg. Chem. 51 (2012) 1827-1836.

[15] F. Brunet, P. Bertani, T. Charpentier, A. Nonat, J. Virlet, Application of ^{29}Si homonuclear and ^{1}H-^{29}Si heteronuclear NMR correlation to structural studies of calcium silicate hydrates, J. Phys. Chem. B 108 (2004) 15494-15502.

[16] P. Rejmak, J.S. Dolado, M.J. Stott, A. Ayuela, ^{29}Si Chemical Shift Anisotropies in Hydrated Calcium Silicates: A Computational Study, J. Phys. Chem. C 117 (2013) 8374-8380.